JNRSE'2022

Bordeaux, 07-08 Juillet 2022

UMR5218

RECUEIL DE RESUMES

JNRSE'2022

Bordeaux, 07-08 Juillet 2022

UMR5218

SPONSORING

JNRSE'2022

Bordeaux, 07-08 Juillet 2022

université de BORDEAUX ims cnrs

UMR5218

CONFERENCES INVITEES

Noëlle Gogneau (C2N Paris-Saclay) - Electromechanical transducers based on GaN nanowires: Influence of the nanometer scale on the properties

Abstract: A new generation of piezoelectric generators based on 1D-nanostructures is appeared, these last years, to develop autonomous power micro-systems. Thanks to their high crystalline quality, their high mechanical properties and their large surface-to-volume, these nanostructures present advantages to significantly enhance the generator conversion efficiency. However, due to their nanoscale dimensions, the nanostructures are also characterized by *"new"* properties, non-significant at micrometric scales, that can lead to a strong modulation of their characteristics. In-depth understanding of these *"new"* properties is thus crucial. Here we use an advanced nano-characterization tool to investigate the relationship between the GaN nanowires characteristics and their piezoelectric conversion properties. The modulation of the free carrier concentration or the formation of nano-contact at the nanowire/electrode interface are examples of the nanoscale phenomena in play.

Speaker's Bio: Noelle Gogneau is a CNRS Research Director at the Center for Nanosciences and Nanotechnologies from Paris-Saclay University. Her research activities are centered on the growth of III-N NWs by Plasma Assisted – MBE and their characterization for Nano-Energy applications, with an emphasis on the development of a new generation of nano/piezo-generators. She is today an expert in the III-N NWs growth and the piezoelectric phenomena involving at nanometer scale. NG takes part to several projects among them the NanoVIBES (Flagship NanoSacalay 2020-24) and SCENIC (ANR-Project (2021-24)) projects as coordinator. She is also currently the chair of the European COST Action OPERA – "European Network for Innovative and Advanced Epitaxy" (2021-25; https://cost-opera.eu/) dedicated to the development of more efficient and cheaper devices and of new devices with new functionalities.

Author of 100 publications, her H-index is 23 (25) from Publon (Google Scholar).

Didier Lasseux (I2M Bordeaux) - Current production in porous microelectrodes: modelling towards an optimal material design.

Abstract: Porous materials are of special interest for the development of electro-devices such as bio-batteries, bio-actuators and bio-sensors, in particular for miniaturization purposes. Because of their potentially large specific area, these materials allow high current density production that can be several orders of magnitude larger than simple flat electrodes of comparable volume. Nevertheless, these materials have always been designed so far on an empirical basis regarding the thickness of the material and its pore size and organization. These parameters have a crucial impact on the competition between mass transfer, enzymatic turn-over and heterogeneous electron transfer rate. A way to progress in their optimization is to make use of modelling, in order to decipher the relationship between the microstructure and the macroscopic properties of the electrode. The presentation will show how this modelling approach through the scales can be performed in conjunction with material reconstruction based on image analysis and electroanalytical tests carried out on synthetized porous materials. Several different electro-chemical situations will be illustrated and an optimization procedure for the electrode macroscale dimensions will be reported. The overall procedure opens the way towards a rational recursive method of an optimal design for efficiency improvement of these devices.

Speaker's Bio: Didier Lasseux is a CNRS Research Director at I2M (Institut de Mécanique et d'Ingénierie – Dpt TREFLE), University of Bordeaux. His research is dediacted to transport phenomena in porous media, with a special accent on modelling at different scales, using upscaling methods. A special focus has been dedicated these last years to coupled transport and electrochemical mechanisms involved in porous electrodes and batteries. Among others, the aim is to elucidate the relationship between the micostructure of the materials and their macroscopic properties. He is the coordinator of the ANR project MOMA (ANR-17-CE08-0005) (MOdeling of Porous Electrodes for an Optimized MAterial Design). He is the co-funder of the International Society for porous media (InterPore), chair of the National Chapters committee of this society, and chair of the France InterPore Chapter (FIC). He authored and co-authored 95 articles in peer-reviewed journals, 6 patents, and around 180 presentations in conferences.

Benoit Guiffard (IETR Nantes) - Flexoelectric energy conversion in soft polymer

Abstract: Flexoelectric effect in matter corresponds to an electrical polarization induced by a strain gradient. This transduction mechanism is expected to be exalted by enlarged strain gradients at small scales and also in the case of flexible compounds like soft polymers, which are able to withstand very large curvature. However, this presently understudied coupling remains weak in comparison with piezoelectric effect in organic films. In this talk we will present the flexoelectric effect in specific polymer films, with flexoelectric coefficients up to 1000 times larger than those actually measured in dielectric polymers, thus possibly allowing an alternative to piezoelectric materials. The methodology consists in using semi-conducting conjugated structures exhibiting high polarizability. Hence, enhancing both the interfacial and ionic polarizations in polymer films with soft treatments is a promising way to induce dipolar motion and free charges transport (i.e. large polarization changes) under strain gradient. The combination of the two functionalities- flexibility and enhanced flexoelectricity- would enable integration of these films in task-oriented devices for low frequency (<100 Hz) mechanical energy conversion.

Speaker's Bio: Prof. B. Guiffard, Nantes University, France, Team co-leader of the « FunMAT » (Functional Materials) team, of the Institute of Electronics and digital Technologies (IETR) Benoit Guiffard joined the LGEF Laboratory at INSA, University of Lyon, France in 1996, where he obtained his Ph.D. degree in inorganic chemistry in 1999. He became an Associate Professor at INSA in 2000 when he worked on doped ferroelectric materials (ceramics, single crystals). His following research interests included the development of electroactive polymer composites exhibiting electromechanical coupling for environmental energy scavenging applications and large electric field actuation performance. In 2011, he has been hired as a Professor at the University of Nantes, France (IETR Lab, Functional Materials group), where he currently works on ferroelectric thin films and flexoelectric polymer composite films. The main target applications are the integration of functional materials in smart sensors and vibrating energy harvesting devices. Prof. B. Guiffard is the co-author of 4 patents, 84 articles

Lionel Hirsch (IMS Bordeaux) - The boost of organic solar cells with Non-Fullerene Acceptors

Abstract: Organic bulk heterojunction photovoltaic solar cells (OPV), with record efficiency approaching 19% and proven high stability, are becoming a credible technology to participate in the global renewable energy bouquet. For more than a decade, only fullerene derivatives were used as electron acceptor materials. This class of materials has good electron transport properties thank to the spherical geometry that enhance the orbital overlap between fullerenes but as their optical absorption is very low, they don't participate to the photogeneration of current. The recent progresses on the OPV power conversion efficiency origin from the synthesis of new electron acceptor materials that combine both electron transport and optical absorption properties. In this context, OPV manufacturers need materials in sufficient quantity and certified quality. Batch-to-batch variations must be eliminated and impurities content should be carefully controlled, could them be organic or metallic traces. This presentation will show a description of the physics of OPV and the organic semiconductors in a first part. In a second part, we will focus on the effects of impurities in the raw semiconductor on solar cells. Our recent research will be presented describing our strategies to identify critical impurities and to estimate the tolerance threshold of solar cell. If initial post-fabrication efficiency of solar cells is obviously examined, our studies also explore the impurity effects on the stability of solar cells under illumination.

Speaker's Bio: Lionel HIRSCH is CNRS director of research working on both organic and perovskite semiconductors-based devices. He has a material science and electrical engineering background and works at the IMS laboratory at the university of Bordeaux. His research interests are focused on the elucidation of charge transport mechanisms in organic semiconductors devices – organic and hybrid perovskite solar cells – organic field effect transistors – Interfaces in organic devices and temperature studies of electro-optical properties – Physico-chemical characterizations. He has published 130 papers in peer-reviewed international journals, 2 patents, 29 invited talks in national and international conferences.

More details are available on https://oembordeaux.cnrs.fr and www.ims-bordeaux.fr

JNRSE'2022

Bordeaux, 07-08 Juillet 2022

université de BORDEAUX

ims

cnrs

UMR5218

ORAUX

Sputtered vanadium nitride films as efficient pseudocapacitive electrodes with high cycling stability

Aiman JRONDI [1,2,3], Kevin ROBERT[1], Pascal ROUSSEL [1,2],Christophe LETHIEN [1,2,4]

[1] *Univ. Lille, CNRS, Centrale Lille, Univ. Polytechnique Hauts-de-France, UMR 8520 - IEMN - Institut d'Electronique de Microélectronique et de Nanotechnologie, F-59000 Lille, France*

[2] *Univ. Lille, CNRS, Centrale Lille, Univ. Artois, UMR 8181 - UCCS - Unité de Catalyse et Chimie du Solide, F-59000 Lille, France*

[3] *CNRS FR 3459, Réseau sur le Stockage Electrochimique de l'Energie (RS2E), 33 rue Saint Leu, 80039 Amiens Cedex, France*

[4] *Institut Universitaire de France (IUF)*

aiman.jrondi@univ-lille.fr

***Abstract*—Microsupercapacitors (MSCs) are considered as promising miniaturised electrochemical energy storage devices for Internet of Things (IoT) applications. The performance of MSCs based pseudocapacitive transition metal nitrides, in particular vanadium nitride "VN" electrode materials, is attracting nowadays a strong attention for showing promising results**[1]**. However, state-of-the-art performance is still needed to meet the energy demand in IoT applications. Thin VN films, deposited by magnetron sputtering in a reactive atmosphere (N_2 and Ar), have been recently explored** [2]**but with a lack of long-term stability. The present study fills the previously observed gaps regarding the electrochemical stability in cycling and the sensitivity of the films in ambient environment (oxidation), by optimising the deposition parameters, in particular, the partial pressure of nitrogen in the plasma. It is shown that tuning these parameters lead to both significantly improved electrical conductivities and electrochemical stabilites, in addition to a minimization of the film oxidation.**

I. INTRODUCTION

Today, the next generation of wireless electronic systems has led to two major challenges: devices miniaturization and fabrication of long term cycling miniaturized energy storage device. Combining a micro-supercapacitor (MSC) with a Li-ion micro-battery (MB) is an attractive solution where the MSC could be used to absorb the current peaks demands (power density) while the MB provides the permanent energy. MSCs are a new class of small electrochemical capacitor where either carbon-based materials or pseudocapacitive ones could be used as efficient thin or thick electrodes. Among the existing pseudocapacitive materials, transition metal nitride materials are an existing playground where various electrodes could be designed and tested in different electrolytes. More specifically, vanadium nitride "VN"[1] has been proposed recently as an electrode with promising results.

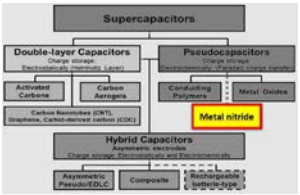

FIGURE 1: THE DIFFERENT TYPES OF MATERIALS THAT MAKE UP THE ELECTRODES OF SUPERCAPACITORS

This compound deposited as thin film by magnetron sputtering deposition method in a reactive atmosphere (N2 and Ar) was recently explored. After a careful optimization of the deposition conditions (working pressure, temperature and thickness), VN was proposed as a bifunctional material (electrode and current collector) with a high volumetric capacitance (1350 $F.cm^{-3}$). Nevertheless, the sputtered VN films only exhibited about 70% capacitance retention after 10,000 cycles[2], which have to be improved to satisfactorily power IoT. In that context, in this study we show that increasing the partial pressure of the nitrogen had a significant influence on the physico-chemical, structural, morphological, and electrochemical properties of the films.

II. METHOD

A. Reactive cathodic magnetron sputtering

Physical vapor deposition (PVD) techniques are widely used in the semiconductor industry for large-scale applications (transistor, memory, solar cells, etc.). Among the existing PVD techniques (molecular beam epitaxy, evaporation, etc.), magnetron sputtering plays an important role in the production of large substrates thin films .

TABLE 1. DEPOSITION TECHNIQUE

Deposition technique	**Reactive cathodic magnetron sputtering**
Fixed parameters	Chamber pressure : 10-2 mbar Deposition temperature : RT Applied power: 150 W DC
N_2 ratio (%) = $\frac{N_2}{N_2+Ar}$	From 5 to 100%N_2 [5, 9, 10, 13, 17, 20, 30, 40, 50, 60, 70, 80, 83, 87, 90, 91, 95, 100%N_2] (18 compositions)

FIGURE 2 : TYPES OF SUBSTRATES USED, (SIN) USED FOR ELECTROCHEMICAL TESTING AND (SIHR) FOR RESISTIVITY (CONDUCTIVITY) TESTING

III. Result

A. Physical properties

Increased nitrogen content leads to denser films; increased conductivity and reduced deposition rate. However, the density and conductivity values are below the polycrystalline theoretical ones ($\rho_{th(powder)}$= 6.1 g.cm^{-3}[3] and $\sigma_{th(thin\ film)}$= 1.6 10^6 S.cm^{-1}[4]).

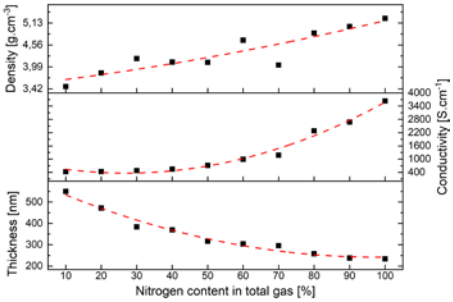

Figure 3 : Evolution of density, conductivity and thickness as a function of nitrogen flow

B. Morphological and structural properties

Depending on the nitrogen content, we go from a porous film to a dense film and from a pyramidal surface to a smooth cauliflower-like surface.

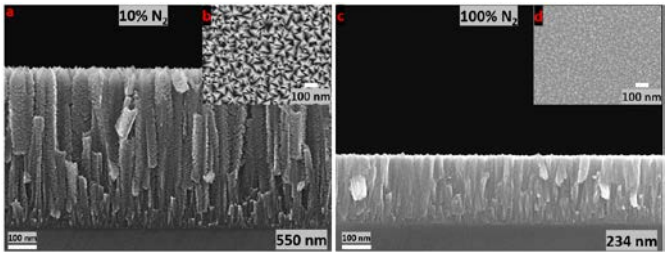

Figure 4 : SEM images showing surface and cross-section morphology, a,b- 10% N_2, c,d-100% N_2

An increase in cell size is also due to the presence of different nitrogen levels in the plasma.

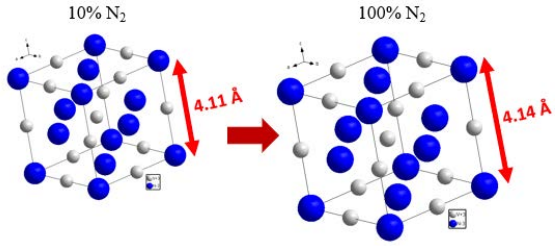

Figure 5 : The expansion of the dimensions (parameter a) of the cubic cell between 10 and 100% N_2

C. Electrochemical properties CV

According to the CV curve at different nitrogen percentages, we visualize on the one hand, the effect of the variation of the conductivity of our films at high scan rate (100mV.s^{-1}), and on the other hand, the decrease of the amplitude of the peaks of oxidation-reduction reactions (characterizing the pseudocapacitance phenomenon).

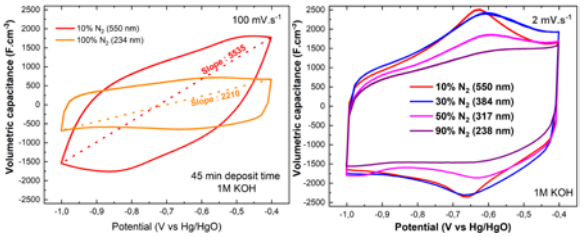

Figure 6 : The curve of cyclic voltametry at high (left graph) and low (right graph) scan rates for different percentages of nitrogen

After optimisation of the deposition parameters, in particular the nitrogen flow in the plasma, the capacitance retention after 10,000 cycles is even higher than 100%. Note also that this film (red square in the figure) was left for 13 months in ambient environnement without any impact on its performances.

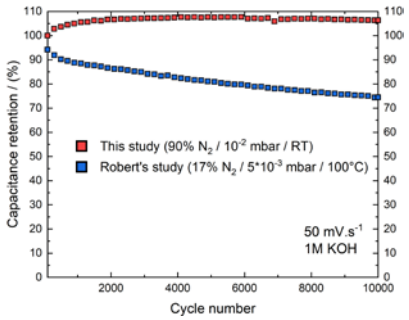

Figure 7: Comparison of electrochemical stability (capacitance retention) between 2018-Robert's results and the current study at different deposition parameters

IV. Conclusion

This study allowed a significant improvement on the film performance, for instance, by increasing the capacitance retention Rc ≥ 99% after 10.000 cycles, and minimizing the films oxidation in ambient environment which was confirmed by an aging study. Finally, the electrical conductivity of the films was increased from 1700[2] to 3600 S.cm^{-1} making the sputtered VN films as an efficient electrodes allowing to deliver high capacitance values with high rate capabilities.

References

[1] D. Choi, G. E. Blomgren, and P. N. Kumta, "Fast and reversible surface redox reaction in nanocrystalline vanadium nitride supercapacitors," *Adv. Mater.*, vol. 18, no. 9, pp. 1178–1182, 2006, doi: 10.1002/adma.200502471.

[2] K. Robert *et al.*, "On Chip Interdigitated Micro-Supercapacitors Based on Sputtered Bifunctional Vanadium Nitride Thin Films with Finely Tuned Inter- and Intracolumnar Porosities," *Adv. Mater. Technol.*, vol. 3, no. 7, 2018, doi: 10.1002/admt.201800036.

[3] T. Y. Kosolapova, *Handbook Of High Temperature Compounds: Properties, Production, Applications*. 1990.

[4] Y. Liu, L. Liu, L. Kang, and F. Ran, "Vanadium nitride with surface single specie oxide via vanadium-organic frameworks precursor," *J. Power Sources*, vol. 450, no. October 2019, p. 227687, 2020, doi: 10.1016/j.jpowsour.2019.227687.

Wideband opportunities of resonant electromagnetic vibration energy harvesters thanks to electrical tuning

G. Delattre[1*], S. Vigne[2], A. Brenes[3], N. Garraud[1], O. Freychet[1], S. Boisseau[1]

[1] *Univ. Grenoble Alpes, CEA, Leti, F-38000 Grenoble, France*

[2] *CEA, DAM, DIF, 91297, Arpajon, France*

[3] *Centre for Nanoscience and Nanotechnology, Univ. Paris Sud–CNRS, Université Paris-Saclay, France*

*gallien.delattre@cea.fr

***Abstract*— This work focuses on the opportunities offered by electrical tuning to widen the bandwidth of Vibration Energy Harvesters (VEH) based on electromagnetic conversion. We show that some electromagnetic transducer topologies are more likely than others to take advantage of the wide bandwidth offered by electrical tuning. Using a general model including both a resonant electromagnetic VEH and a resistive-capacitive interface with electrical tuning, we highlight the parameters of interest influencing the bandwidth of the system. Based on these results, we develop a generic optimization approach suitable for any electromagnetic transducer topology. The full optimization of different transducer topologies shows that the one that is based on variable reluctance is the best in terms of bandwidth-related performances.**

I. Introduction

Vibration Energy Harvesters (VEH) are an efficient way to supply low power electronics by converting mechanical energy into electricity. However, their adoption remains very limited because of their frequency selectivity. To overcome this issue, some researchers has developed a method called electrical tuning, which consists in adding a dynamic load-matching interface to the VEH in order to maximize the power transferred to the load at any frequency [1], [2].

In this work, we focus on VEH based on electromagnetic transduction to perform the electromechanical conversion. Various topologies of electromagnetic transducers have been reported in the literature. The simplest ones (type 1) are designed with magnets in motion relative to a winding [3]. Some others (type 2) include additional parts, mechanically connected to the magnets and made of a soft-ferromagnetic material, which allow to channel the magnetic flux lines [4]. Still others (type 3, sometimes referred to as variable reluctance transducers) are composed of magnetic circuits involving magnets, coils, and air-gaps whose variation leads to magnetic flux changes in the circuit [2], [5].

The general objective of this work is to determine which kind of electromagnetic transducer topology achieves the best performances in terms of bandwidth when combined with an electrical tuning strategy. To meet this objective, we first propose three representative topologies of electromagnetic transducers (Section 2.). We then present a general model of electrically-tuned electromagnetic VEH, and introduce normalized parameters (Section 3.). Lastly, we develop a generic optimization approach to compare the three topologies and conclude about the bandwidth opportunities offered by them (Sections 4. and 5.).

II. Presentation of three topologies of electromagnetic transducers T1, T2 and T3

The three proposed topologies of electromagnetic transducers, T1, T2 and T3, correspond respectively to the types 1, 2 and 3 evoked in Section 1, and are depicted in Figure 1.

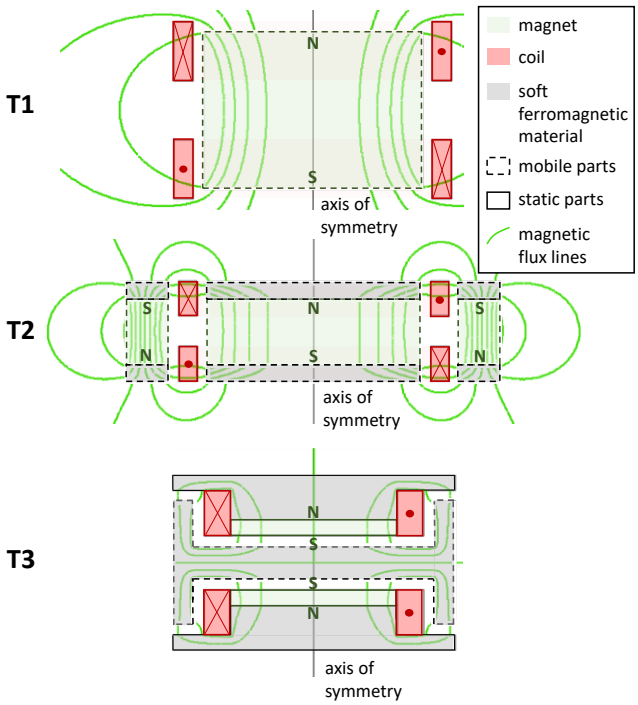

FIGURE 1. SCHEMATIC REPRESENTATION OF THE THREE PROPOSED TOPOLOGIES OF ELECTROMAGNETIC TRANSDUCERS

For each topology, the mobile part is connected to the static part with a spring (not represented), which ensures the guidance of the mobile along the axis of symmetry.

III. Model of resonant electromagnetic VEH

In small displacements condition, resonant electromagnetic VEH are ruled by the linear system of equations (1):

$$\begin{cases} M \cdot \dfrac{d^2x}{dt^2} + D \cdot \dfrac{dx}{dt} + K \cdot x + \beta \cdot i = -M \cdot a \\ v + R_c \cdot i + L_c \cdot \dfrac{di}{dt} = \beta \cdot \dfrac{dx}{dt} \end{cases} \quad (1)$$

M, D, and K correspond to the mobile mass, the mechanical damping and the stiffness of the mechanical resonator respectively. β is the transduction coefficient of the gyrator performing the electromechanical conversion. R_c and L_c represent the coil resistance and inductance respectively. a, x, v and i stand for the input acceleration, the mobile displacement in relation to its equilibrium position in the referential of the vibrating frame, the output voltage and current in the winding, respectively.

To implement electrical tuning, adjustable resistive and capacitive loads, R_{load} and C_{load}, are connected to the VEH output. This results in equation (2):

$$v + R_{load}C_{load}\frac{dv}{dt} = R_{load} \cdot i \qquad (2)$$

The electrical power transferred to R_{load} constitutes the power output of the electrically-tuned VEH. The real time adjustment of C_{load} and R_{load} allows to maximize this power at any frequency, and hence enlarge the effective bandwidth of the VEH. For a given acceleration amplitude $|a|$ and a given transducer volume V, the effective bandwidth over which the VEH delivers a certain power level P_0 can be expressed in terms of four normalized parameters, which are listed in Table 1 (analytical developments not shown).

TABLE 1. NORMALIZED PARAMETERS

characteristic parameter	***expression***	***unit***
resonant frequency	$\omega_0 = \sqrt{K/M}$	$[\mathrm{rad \cdot s^{-1}}]$
effective density	$\rho = M/V$	$[\mathrm{kg \cdot m^{-3}}]$
quality factor	$Q = \sqrt{KM}/D$	$[-]$
electromagnetic coupling density	$\Gamma = \beta^2/(R_c V)$	$[\mathrm{kg \cdot s^{-1} \cdot m^{-3}}]$

To increase the bandwidth, electromagnetic VEH with large ρ, Q and Γ should be sought, and low frequencies applications, involving low ω_0, should be preferred.

IV. OPTIMIZATION AND RESULTS

For each topology, we propose to perform a shape optimization in order to maximize ρ and Γ, while ω_0 and Q are left out of the optimization procedure. Until a certain targeted power level P_0 is specified, it is not possible to find a unique optimal shape of a given topology, because there is a trade-off between ρ and Γ. But we can get a comprehensive view of its performances by using the following optimization criteria (3) for $n \geq 1$:

$$\mathcal{C}_n = \Gamma^{\frac{1}{n}} \cdot \rho^{1-\frac{1}{n}} \qquad (3)$$

Setting $n = 1$ is equivalent to focus exclusively on Γ in the optimization process, and leads to a larger bandwidth at the expense of the harvestable power levels. Greater values of n leads to higher harvestable power levels at the expense of the bandwidth. In this work, using the commercially-available softwares Altair HyperStudy® and Altair Flux®, we have run 8 optimizations ($n \in [\![1, 8]\!]$) for each transducer topology. This results in 8 different shapes, which can then be plotted in terms of ρ and Γ (Figure 2).

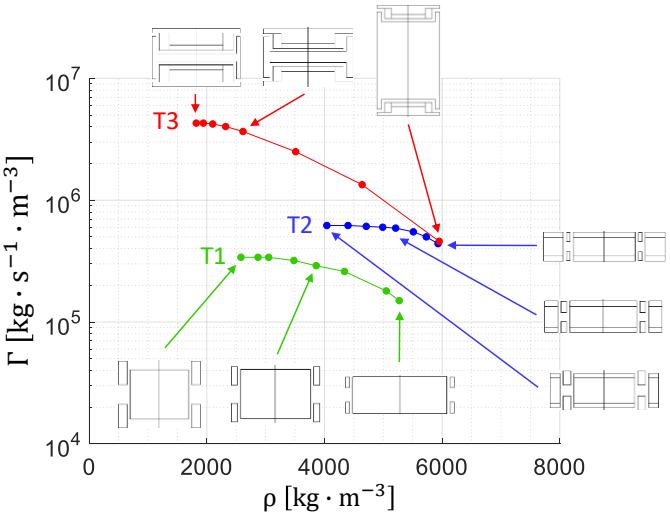

FIGURE 2. PLOT OF OPTIMAL Γ AND ρ FOR EACH ELECTROMAGNETIC TRANSDUCER T1, T2 AND T3

Figure 2 allows us to compare the three topologies in a fair manner, since they are composed of the same materials and they are fully optimized in terms of ρ and Γ. It clearly appears that T3 performs better than T2, and T2 performs better than T1. For the sake of illustration, we consider the case of [4], where $|a| = 4.16\ \mathrm{m \cdot s^{-2}}$, $V = 0.676\ \mathrm{cm^3}$, $Q = 38$ and $\omega_0/2\pi = 59$ Hz. At $P_0 = 234\ \mu\mathrm{W}$, the normalized bandwidth of T1 is 7.4 %, the one of T2, 11.5 %, and the one of T3, 15.9 %. With a normalized bandwidth 1.4 and 2.1 times higher than the ones of T2 and T1 respectively, the superiority of T3 is then clearly noticeable.

V. CONCLUSION

In this work, we have proposed three representative topologies of electromagnetic transducers in view to optimize them and compare their bandwidth when combined with an electrical tuning strategy. The transducer T3, based on variable reluctance, appears to perform significantly better than the two others. Electromagnetic transducers based on variable reluctance are therefore an interesting approach to develop wideband vibration energy harvesters.

REFERENCES

[1] A. Cammarano, S. G. Burrow, D. A. W. Barton, A. Carrella, et L. R. Clare, « Tuning a resonant energy harvester using a generalized electrical load », *Smart Mater. Struct.*, vol. 19, n° 5, p. 055003, mars 2010, doi: 10.1088/0964-1726/19/5/055003.

[2] D. Zhu, S. Roberts, T. Mouille, M. J. Tudor, et S. P. Beeby, « General model with experimental validation of electrical resonant frequency tuning of electromagnetic vibration energy harvesters », *Smart Mater. Struct.*, vol. 21, n° 10, p. 105039, sept. 2012, doi: 10.1088/0964-1726/21/10/105039.

[3] N. G. Elvin et A. A. Elvin, « An experimentally validated electromagnetic energy harvester », *J. Sound Vib.*, vol. 330, n° 10, p. 2314-2324, mai 2011, doi: 10.1016/j.jsv.2010.11.024.

[4] D. Mallick et S. Roy, « Bidirectional electrical tuning of FR4 based electromagnetic energy harvesters », *Sens. Actuators Phys.*, vol. 226, p. 154-162, mai 2015, doi: 10.1016/j.sna.2015.02.016.

[5] J. Bjurström, F. Ohlsson, A. Vikerfors, C. Rusu, et C. Johansson, « Tunable spring balanced magnetic energy harvester for low frequencies and small displacements », *Energy Convers. Manag.*, vol. 259, p. 115568, mai 2022, doi: 10.1016/j.enconman.2022.115568.

Efficient Impulse-Driven Electromagnetic Energy Harvesting for Tire Pressure Monitoring Systems

Maxim Germer[1,*], Uwe Marschner[1] and Andreas Richter[1]

[1] *Technical University of Dresden, Chair of Microsystems, Nöthnitzer Str. 64, 01187 Dresden, Germany*

*maxim.germer@tu-dresden.de

Abstract—**Energy harvesting (EH) for tire pressure monitoring systems (TPMSs) is a key element to make tire sensors self-sufficient and to provide the necessary energy for next generation TPMS. This work studies an electromagnetic energy harvester (EMEH) system with interface circuit, which is connected to a 220-µF capacitor as energy storage. The EH has been optimized to work especially at low vehicle velocities. Since EMEHs suffer from a low output voltage at low velocities, a voltage tripler has been used to up-convert the voltage and to increase the efficiency along the whole capacitor voltage range compared to Standard Energy Harvesting. Measurements on a tire test rig delivered excellent experimental results. A comparison with experimentally validated impulse-driven tire based state-of-the-art systems reveals an overall performance increase of 300 % and 1500 % at the critical vehicle velocities of 20 km/h and 30 km/h, respectively.**

I. Introduction

Energy harvesting (EH) for tire pressure monitoring systems (TPMSs) is a key element to make tire sensors self-sufficient and to provide new features for future vehicle tires. Manifold impulse-driven energy harvester systems, mainly of piezoelectric nature and with beam structures, have been studied for TPMSs and used the change in centrifugal acceleration [1-4]. The disparity between generated electrical energy and power on the one hand and demanded energy and power on the other hand necessitates the use of a temporary storage. A 220-µF capacitor, which has been charged to 3.9 V, provides enough energy for measurements and data transmission. The required energy normalized to one revolution E_{rev} is described in [5]. It is 4.6 µJ/rev in driving mode and 7.9 µJ/rev when the storage is empty after a long parking period.

Piezoelectric systems have been mostly studied for TPMS due to their high voltages at low impulse amplitudes. If embedded on the tire innerliner, they suffer from fragility at high velocities, though [5]. Contrary, electromagnetic energy harvesters (EMEHs) as described in [6,7] with a nonlinear magneto-mechanical spring are more robust. Due to low impulse amplitudes at $v \leq 25$ km/h, at which the TPMS needs to be operational [8], the output voltage are too low to charge the storage to 3.9 V. A step-up converter, placed between EH output and capacitor, is used to raise the voltage.

Efficient boost-converters with an AC-DC converter rectify and raise the output voltage. Recent techniques are presented in [9-11]. Usually, a switch short-circuits and open-circuits the inherent inductor of the EMEH. Because of the current continuity of the inductor, the EMEH is able to charge the capacitor independently of its actual voltage. These circuits are typically implemented as integrated circuits. According to [11], the optimal switching time depends on the resistance and inductance of the inherent inductor and requires customization. A simple but less efficient alternative to these customized and complex circuits are voltage multipliers which raise the open-circuit voltage by multiple times.

The purpose of this work is to study the performance of an EMEH with voltage multiplier and to compare it to recent solutions.

II. Electromagnetic Energy Harvesting System

The herein studied EMEH builds on the work of [6,12], in which a movable magnet was placed in a housing, levitated by a fixed magnet with an opposite magnetic field. A single coil was wound around the housing. At both ends of the housing elastic bumpers were added. Two coils were used to transform the magneto-mechanical energy into electrical energy. The originally system delivered only $v \geq 50$ km/h peak voltages above 2 V. Contrary, this work, intends to provide higher peak voltages to guarantee the function of TPMSs at $v \geq 25$ km/h.

The electromagnetic energy harvester is illustrated in Fig. 1 and uses the impulses in the area of tire ground contact. To obtain a low mechanical damping, the housing is made out of PTFE and air channels are milled inside the tube to reduce pressure damping as described in [13]. The electromagnetic coupling coefficient is nonlinear with a maximum in the central housing position [14]. The fixed magnet has been chosen to centrally align the movable magnet at 25 km/h and to tune the output voltage at this velocity. The system parts have been modelled with FEM and experimentally validated separately with a tensile test machine and with a test setup, consisting of laser triangulation sensor and of a voltmeter to determine the distance-dependent coupling coefficient β by $\beta(z) = u(z)/v(z)$, where $u(z), v(z)$ are voltage and velocity of the movable magnet at the position z.

Electromagnetic energy harvester prototypes with 2 x1060 coil turns have been designed to fit in the rubber container of a tire based TPMS. The linearized properties are listed in Tab. 1.

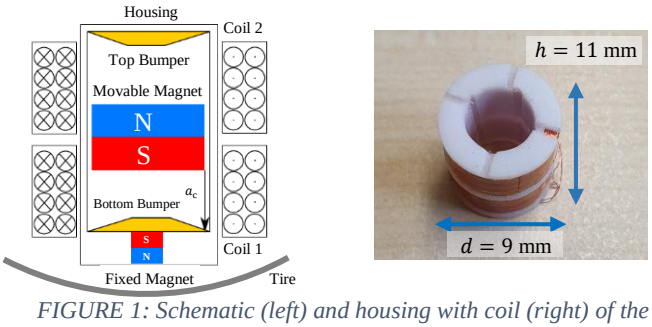

FIGURE 1: Schematic (left) and housing with coil (right) of the TPMS electromagnetic energy harvester

Table 1: Linearized electromechanical system parameters at 25 km/h

Coil wire	d	0.071	mm
Number of turns per coil	N	1060	
Total resistance	R_c	262	Ω
Total inductance	L_c	12	mH
Storage capacitor	C_s	220	µF
Electromagnetic coupling coefficient	β	6	Vs/m
Damping coefficient	c	0.21	kg/s
Mass	m	0.85	g
Magneto-mechanical stiffness	k	77	N/m

III. Voltage Mulitplier

The low output voltage of the energy harvester can be increased with a voltage multiplier. The multiplier voltage U_{MP} is expressed as

$$U_{\mathrm{MP}} = n\,(U_0 - U_{\mathrm{d}}), \qquad (1)$$

where n, U_0, U_{d} are number of multiplier stages, open-circuit voltage and diode forward voltage. To obtain an output $U_{\mathrm{MP}} > 3.9$ V, while $U_0 \approx 2$ V ($v = 25$ km/h) and $U_{\mathrm{d}} = 0.3$ V for a schottky diode, the number of stages is $n = 3$. Correspondingly, a voltage tripler (VT) is used as interface circuit and connected to the capacitor C_s as illustrated in Fig. 2.

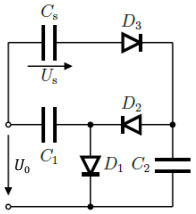

FIGURE 2: Voltage tripler with storage for step-up conversion

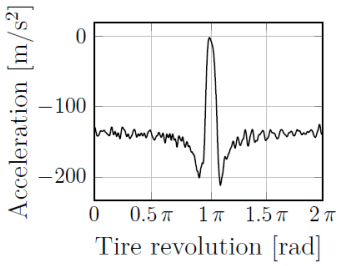

FIGURE 3: Tire wave signal at the tire innerliner at 25 km/h

LTspice simulations of the equivalent electromechanical network [14] with the tire wave signal as input, as depicted in Fig. 3, have revealed that the circuit provides the best performance, when the capacitors are $C_1, C_2 = 47$ µF.

IV. Experimental Results

The EMEH prototypes were embedded in a tire, following the preparation steps explained in [5]. Here, Continental Performance Contact 6 20555R16 tires were used for measurements on a test rig as shown in Fig. 4. The wire output of each energy harvester was soldered to the wires of a slip ring.

FIGURE 4: Tire test rig (left) with embedded prototype (right)

Different tests were driven at 3000 N load: First, the open-circuit voltage was measured over many tire revolutions in the range from 20 km/h to 200 km/h and the available energy per revolution has been calculated from the output voltage with $E_{\mathrm{rev,max}} = \int_{t_0}^{t_0+T} U_0(t)/(4R_c)\,\mathrm{d}t$. This quantity has been calculated supposing different forward voltages U_b. The amount of energy $E_{\mathrm{rev}}(|u(t)| > U_b)$ is presented in Fig. 5. As expected, the generated electrical energy increases from 20 km/h on, because the centrifugal acceleration increases significantly. The energy attains a local maximum at 40 km/h and decreases because the period of one tire revolution and the impulse width are inversely proportional to the velocity, whereas the EMEH resonance frequency is only slightly affected. Comparing the energy for $U_b = 0$ V and $U_b = 0.6$ V shows that almost half of the energy will be dissipated due to the small signal amplitude and noise for $v \leq 30$ km/h.

In the second test, the VT with storage was connected to the EH output and the voltage of the capacitor was measured. The energy E_{rev} was deduced from the voltage signal and compared to state-of-the art results as illustrated in Fig. 6. The EMEH with VT outperforms the other state-of-the-art EH. At 20 km/h and 30 km/h, the transducer improves the provided energy by 300 % and 1500%, respectively. The power transfer efficiency of the EMEH with VT reached up to 50 % and can be increased with switching boost circuits. In addition, no system reliability issues occurred during tests of a few tens of km, and the generated E_{rev} is large enough for higher velocities greater than 30 km/h.

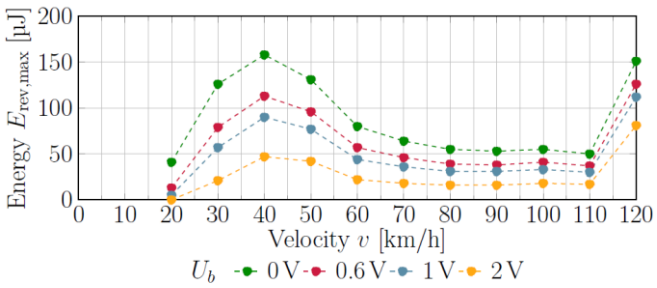

FIGURE 5: Maximal available energy above the forward voltage U_b

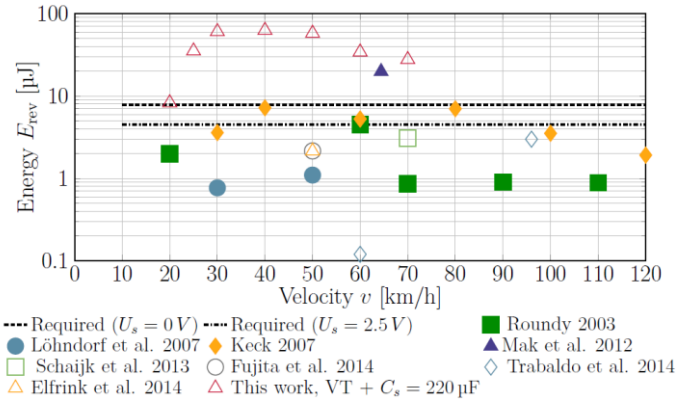

FIGURE 6: Comparison of recent experimentally validated impulse-driven energy harvesters with this work (red triangles)

V. Conclusion

This study has presented a nonlinear EMEH specifically designed to provide enough energy at 25 km/h. A voltage tripler has been used to step-up convert the low output voltage and to charge a storage to 3.9 V within less than one minute. Experimental validation has shown a performance increase of 300 % and 1500 % at the critical low velocities of 20 km/h and 30 km/h compared to the best published and experimentally validated systems.

References

1 S Roundy, 2003, PhD thesis
2 M. Keck, 2007, *IEEE* Sensors
3 T. Fujita et al., 2014, Procedia Engineering
4 E. Trabaldo et al., 2014, Journal of Physics: Conference Series 557
5 M. Germer et al., 2022, *IEEE* Internet of Things Journal
6 S. Tornincasa et al., 2011, JIMSS Journal, Vol. 23, No. 18
7 C. Saha et al., 2008, Sensors and Actuators A: Physical
8 Standard ISO:21750 , 2006
9 E. Bonisoli et al., 2017 IEEE/ASME Transaction on Mechatronics, Vol. 22, No. 5
10 A. Quelen et al., 2020, IEEE International Solid-State Circuits Conf., Session 32.3
11 M. Germer et al., 2021 JNRSE
12 E. Bonisoli et al., 2010 *IEEE* Transactions on Magnetics, Vol. 46, No. 5
13 S. Tornincasa et al., 2011 JIMSS Journal, Vol. 23, No. 1
14 M. Germer et al., 2020 SMASIS Conf., No. 2407

Load resistance impact on the electromechanical dynamic of bistable piezoelectric energy harvesters

Quentin DEMOURON[1,*], Adrien MOREL[1], David GIBUS[1], Aya BENHEMOU[1] and Adrien BADEL[1]

[1] *Univ. Savoie Mont Blanc, Laboratoire SYMME, 74940 Annecy-le-Vieux, France*

**Corresponding author: quentin.demouron@univ-smb.fr*

***Abstract*—Bistable piezoelectric energy harvesters are prominent solutions in the field of vibration energy harvesting due to their broadband behavior. However, the impact of the electrical interface and especially the load impedance needs to be addressed. In this paper, the impact of the load resistance on the electromechanical dynamic of the harvester has been studied. Experimental tests allowed us to demonstrate that the load resistance induces an electrical damping allowing to tune the bandwidth of the harvester as well as the harvested power. The results presented in this paper should be considered for the future development of harvested power optimization algorithms as well as orbit jump strategies.**

I. Introduction

During the last decades, there has been a growing interest for new energy harvesting solutions that could enable the development of battery-less sensor nodes. Piezoelectric energy harvesters (PEH) are of particular interest because of their high energy density and their integration capability. The dynamic of PEH can be modelled by a simple set of differential equations according to [1]. Since the piezoelectric energy harvester exhibits a bidirectional electromechanical coupling, it has been proven that the electrical interface has a certain impact on the behavior of the system.

Previous works focused on the load resistance impact on the bandwidth for linear piezoelectric energy harvesters [2] and non-linear monostable piezoelectric energy harvesters [3]. The works presented in [4] focused on the load resistance optimization in order to maximize the harvested power for bistable PEH. However, to date, there is no experimental analysis of the impact of the load resistance on bistable PEH.

In this paper, we propose an experimental study of the load resistance impact on the harvested power as well as on the bandwidth of the bistable PEH. First, we present the experimental testbench. In a second time, the experimental protocol is presented. The experimental measurements are finally discussed.

II. Experimental testbench

In this paper, we focus on a bistable PEH made of an inertial mass connected to two parallel buckled beams. The beams are clamped on one side and connected to an amplified piezoelectric actuator (APA) on the other side as depicted in Fig. 1. The APA is built around a stack of lead titano-zirconate piezoelectric ceramic (PZT) installed in a metallic shell.

An experimental testbench, depicted in Fig. 2, including a dSpace real time interface, an electromagnetic shaker and its associated power amplifier, a differential laser vibrometer and a programmable decade box as been set up. The PEH depicted in Fig. 1 is fixed to the shaker. In order to measure the acceleration amplitude of the excitation signal, an accelerometer is also fixed to the shaker. The dSpace interface is controlled through Matlab scripts and sends control signals to the decade box and the power amplifier driving the shaker. A differential laser vibrometer is used to measure the displacement and speed of the mass of the electromechanical harvester. The piezoelectric voltage is transferred to the dSpace interface by mean of a voltage follower in order to isolate the PEH from the dSpace interface input impedance.

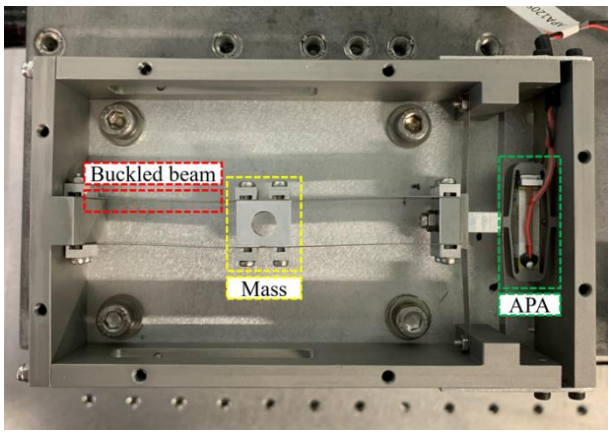

FIGURE 1. Bistable piezoelectric energy harvester

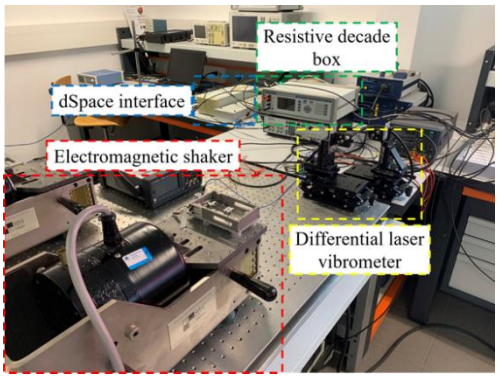

FIGURE 2. Experimental testbench

III. Experimental protocol

Bistable PEH might exhibit two types of motion: intra-well and inter-well motions. Intra-well motion consists in small

oscillations of the inertial mass around one of the two stable positions whereas inter-well motion consists in oscillations around the two stable positions. The experimental characterization is performed on the inter-well motion also known as high-energy orbit. The PEH is submitted to a sinusoidal acceleration of amplitude $\gamma_m = 5\ m.s^{-2}$ and the vibration frequency is swept from 30 Hz to 120 Hz. In order to force the inter-well motion operation of the energy harvester, an orbit jump sequence has been developed. The acceleration amplitude is progressively increased up to 17 $m.s^{-2}$. Under such large vibration amplitude, the PEH starts operating in inter-well motion. Finally, the acceleration amplitude is slowly brought back to $\gamma_m = 5\ m.s^{-2}$ so that the PEH remains in inter-well operation even though the acceleration amplitude is smaller.

The aforementioned orbit jump sequence and frequency sweep are performed for 70 load resistances (from 100 Ω to 30 $k\Omega$). The voltage, displacement, speed and acceleration waveforms are stored for each combination of resistance and vibration frequency.

IV. Results and Discussion

Fig. 3 illustrates the impact of the load resistance on the dynamic of the bistable PEH. It can be seen that the cut-off frequency of inter-well motion f_c is a function of the resistance. For small resistance values ($R < 200\ \Omega$) or large resistance values ($R > 20\ k\Omega$), this cut-off frequency is close to 70 Hz. However, we can observe that f_c decreases until it reaches a minimum of 50 Hz when the resistance is close to 1409 Ω.

Indeed, this resistance is equal to $R = \frac{1}{2C_p\omega}$ (with C_p being the capacitance of the piezoelectric material and ω the angular frequency of the vibration) which maximizes the electrical damping. f_c decreases with the damping which explains that the PEH with a resistance value close to 1409 Ω exhibits a relatively low cut-off frequency whereas a PEH connected to a low damping resistance (e.g. 100 Ω or 30 kΩ) exhibits a relatively high cut-off frequency (70 Hz).

The harvested power depends on the electrical damping associated to the resistance value. We can observe that the harvested power reaches two maxima for two resistances ($R = 1012\ \Omega$ and $R = 2964\ \Omega$). These two resistances allow to reach an electrical damping equal to the mechanical damping, thus maximizing the harvested power. If the resistance is close to 1409 Ω, the electrical damping is greater than the mechanical damping. The system is therefore overdamped and the harvested power slightly decreases. Conversely, if the resistance is larger than 2964 Ω or smaller than 1012 Ω, the electrical damping is lower than the mechanical damping which explains that the harvested power also decreases.

These experimental results prove that it is possible to adjust the harvested power and the critical angular frequency by tuning the load resistance. If the resistance is finely tuned for each vibration frequency, it is possible to harvest more than 1 mW over a frequency band from 30 Hz to 70 Hz as illustrated in Fig. 4. This result demonstrates the wideband behavior of the bistable harvester as well as the interest for designing adaptative electrical interfaces for which the input impedance is dynamically optimized as a function of the vibration.

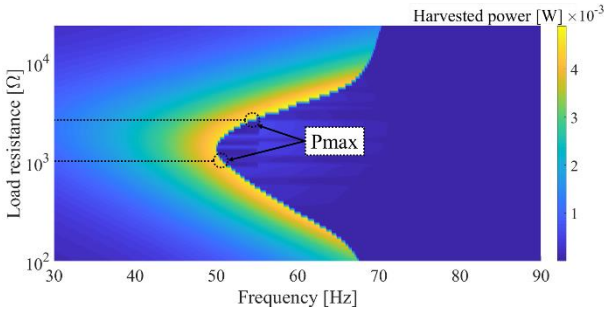

FIGURE 3. HARVESTED POWER AS A FUNCTION OF THE FREQUENCY AND THE LOAD RESISTANCE

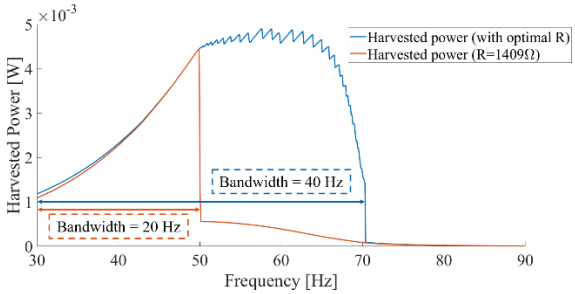

FIGURE 4. MAXIMUM HARVESTED POWER AS A FUNCTION OF THE FREQUENCY

V. Conclusion

In this paper, we presented the impact of the load resistance on the dynamic of the bistable piezoelectric energy harvester for the high-energy orbit. We experimentally proved that the optimal electrical damping which maximizes the harvested power is associated to a load resistance. Moreover, we showed that it is possible to tune the electrical damping of the system by tuning the load resistance, thus optimizing the bandwidth and the harvested power. Considering the presented results, a maximum power point tracking algorithm and an orbit jump strategy aimed at fully exploiting the potential of bistable PEH will be developed and implemented.

Acknowledgment

This project has been supported by the French government, under the Future Investment Program (Programme d'investissements d'avenir).

References

[1] T. Huguet, A. Badel, et M. Lallart, « Parametric analysis for optimized piezoelectric bistable vibration energy harvesters », Smart Mater. Struct., vol. 28, nº 11, p. 115009, nov. 2019, doi: 10.1088/1361-665X/ab45c6.

[1] A. Morel, A. Badel, R. Grézaud, P. Gasnier, G. Despesse, et G. Pillonnet, « Resistive and reactive loads' influences on highly coupled piezoelectric generators for wideband vibrations energy harvesting », Journal of Intelligent Material Systems and Structures, vol. 30, nº 3, p. 386-399, févr. 2019, doi: 10.1177/1045389X18810802.

[3] C. Lan, Y. Liao, G. Hu, et L. Tang, « Equivalent impedance and power analysis of monostable piezoelectric energy harvesters », Journal of Intelligent Material Systems and Structures, vol. 31, nº 14, p. 1697-1715, août 2020, doi: 10.1177/1045389X20930080.

[4] S. Bae et P. Kim, « Load Resistance Optimization of a Broadband Bistable Piezoelectric Energy Harvester for Primary Harmonic and Subharmonic Behaviors », Sustainability, vol. 13, nº 5, p. 2865, mars 2021, doi: 10.3390/su13052865

JNRSE'2022

Bordeaux, 07-08 Juillet 2022

UMR5218

POSTERS

A Low-Power Microcontroller-Based Power Management Circuit with a two-measurements MPPT

Nicolas DECROIX[1,2,*], Pierre GASNIER[1] and Adrien BADEL[2]

[1] *Univ. Grenoble Alpes, CEA, LETI, Grenoble, France*

[2] *SYMME, Univ. Savoie Mont Blanc, Annecy, France*

*nicolas.decroix@cea.fr

***Abstract*—This paper describes a low power implementation of a MPPT algorithm for weakly and moderately coupled piezoelectric energy harvesters (PEH). This "two-measurements" algorithm has been tested with the half-bridge SEH extraction technique (HB-SEH). Each time the input vibration frequency is modified, a microcontroller measures and generates an equivalent resistance at the optimal value ($\pm$ 15%), which gives an input power larger than 95% of the maximum harvestable power. The first tests have shown that the proposed system and its MPPT consume only 7µA @ 1.8V with a STM32L011 microcontroller.**

I. Introduction

Vibration energy harvesting is a promising candidate for powering wireless sensor nodes for IoT. However, the power output of these harvesters heavily depends on the input mechanical conditions (vibrations amplitude and frequency) as well as the unavoidable harvester's variations due to its aging or environment variation (temperature variation mainly). To convert vibration into electricity, piezoelectric-based harvesters are very attractive for their high power density at small scale [1] and their high output voltages as compared with electromagnetic converters. Piezoelectric energy harvesters (PEH) are classically qualified as weakly or strongly electromechanically coupled. This paper focuses on the weakly coupled PEH: Less efficient, but more common and cheaper than strongly coupled. Energy harvesting techniques are necessary to harvest the electrical power from the PEH. One classical technique is called Standard Energy harvesting (SEH) which is made of a full bridge rectifier and a rectifying capacitor. As the power extracted with this technique heavily depends on the output resistor of the PEH, Maximum Power Point Tracking (MPPT) algorithms must be implemented to harvest power for any input acceleration.

MPPT algorithms for weakly coupled algorithms can be divided in two categories: Perturb and Observe (P&O) and Open Circuit-Voltage (OCV) algorithms. The P&O algorithms continuously monitors the output power of the system and consequently adapts the output load of the harvester. These algorithms are often slow to reach their maximum power point [2]. OCV algorithms consists of measuring the open circuit voltage of the PEH, the maximum power is reached at half this open-circuit voltage in the case of SEH. There is no power transmitted to the load while the OCV algorithm is performed and a DC voltage must be regulated, which is not robust to acceleration amplitude changes [3]. Moreover, the displacement of the PEH in open-circuit is higher than when connected to a load, which can be limiting factor from a technological point of view.

In this paper, we propose a low-power implementation of two-measurements impedance estimation for weakly coupled PEH.

II. Model and Method

The PEH associated with the half-bridge SEH (HB-SEH) harvesting technique is also called voltage doubler [3]. This technique is similar to the SEH technique but with an optimal load equal to four times the one of SEH [4] in the case of weakly coupled PEH. In our case, the optimal load is emulated thanks to a flyback-type DC/DC converter. The discontinuous conduction mode control is adopted so that the emulated input resistance of the converter (R_{in}) only depends on its switching frequency (f_{clock}) and its duty cycle ($t_{on} \times f_{clock}$) as given by Eq. (1) :

$$R_{in} = \frac{2L_p}{f_{clock}\, t_{on}^2} \tag{1}$$

with t_{on} the conduction time of the flyback primary side (K_p and L_p, as shown in FIGURE 1). A low-power microcontroller (a STM32L011 in our work) generates the control signal on K_p's gate. A low-power clock (100 kHz) feeds the microcontroller timer to create a fixed t_{on} PWM. We chose a fixed t_{on} control as it enables lower clock frequencies for the same range of emulated load [2], thus reducing power consumption. A schematic of the global system is shown in FIGURE 1.

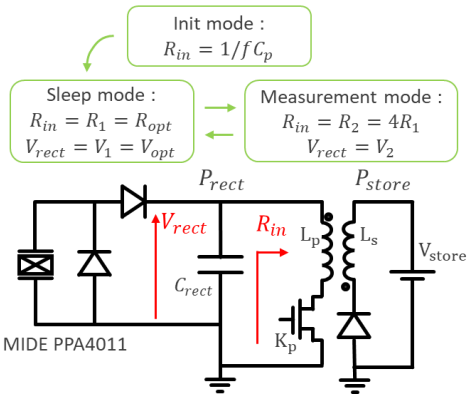

FIGURE 1 : ARCHITECTURE OF THE SYSTEM : MPPT FUNCTIONALITY AND HARVESTING TECHNIQUE

The two-measurements MPPT is based on [5] and similar to [6] insofar as it consists of a simplified impedance measurement. In this work, the measurement is performed with only two voltage measurements on capacitor C_{rect}. The two voltage measurements V_1 and V_2 are performed at two different emulated

loads (R_1, R_2), allowing the calculation of an estimated optimal resistive load $R_{opt-MPPT}$ thanks to Eq. (2).

$$R_{opt-MPPT} = \frac{(V_2 - V_1)R_1R_2}{V_1R_2 - VS_2R_1} \quad (2)$$

This method assumes that the PEH characteristic is linear for a given harvesting technique. In our case, the first emulated load R_1 is assumed to be the optimal load of the system, calculated during the previous cycle of the MPPT algorithm. R_2 is chosen relatively close to R_1 to optimize the power extraction during the second measurement maintaining the operation of the system around the maximal power point.

III. Measurements

To validate our method, we used a MIDE PPA4011 with a 38 g (2 magnet disks of 25mm diameter x 5mm) inertial mass for the first experiments, set on an electromagnetic shaker driven to generate a sinusoidal acceleration whose amplitude is 0.4 $m.s^{-2}$. Its parasitic capacitance is approximately 400nF and the system's coupling is $km^2 = 4\%$ ($km^2Q = 1.6$). As a first approach, we set the first emulated resistance to $R_1 = 1/(f_{piezo}C_p)$, i.e the optimal load outside resonance for the HB-SEH technique, and $R_2 = 4R_1$ for each frequency. For 35 input vibration frequencies (43 Hz to 50 Hz), the system automatically measures and generates an estimated optimal load ($R_{opt-MPPT}$). For those tests, we measured the electrical powers before the flyback converter ($P_{rect-MPPT}$) and the converted powers on the storage capacitor ($P_{store-MPPT}$) at the flyback output (FIGURE 2). These power measurements were compared to those obtained with the optimal, manually found, discrete resistive loads ($P_{opt-RES}$ @ $R_{opt-RES}$) connected to C_{rect} instead of our system. The estimated optimal loads ($R_{opt-MPPT}$) are plotted and compared to the discrete optimal loads ($R_{opt-RES}$) in FIGURE 3.

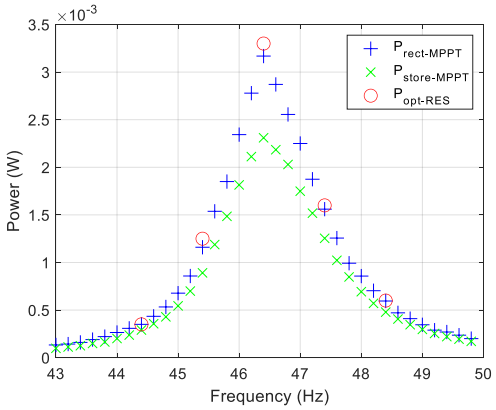

FIGURE 2 : ELECTRICAL POWERS OBTAINED WITH THE PROPOSED MPPT ($P_{RECT-MPPT}$ AND $P_{STORE-MPPT}$) AT 0.4G COMPARED TO THE OPTIMAL POWER ON DISCRETE RESISTIVE LOADS ($P_{OPT-RES}$)

We can see that the electrical powers upstream of the flyback are very close to $P_{opt-RES}$. It should be mentioned that the efficiency of the flyback (85% max - 73% min) has not been optimized yet. One can also note that the resistance values estimated by the algorithm follow the same trend and are relatively close to the discrete optimal loads. Further measurements are currently underway. It is complicated to see a clear relationship between the optimal load $R_{opt-RES}$ and the one obtained by the MPPT algorithm ($R_{opt-MPPT}$) as the PEH for our experiment was weakly coupled and thus slightly impacted by load variations.

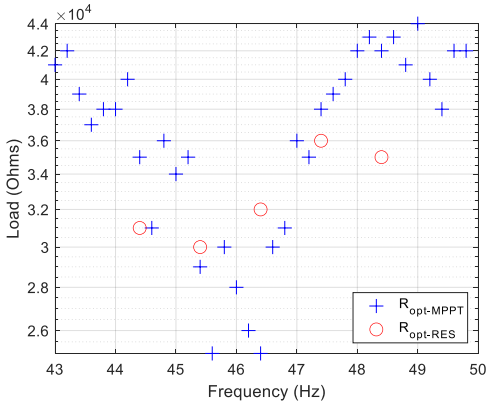

FIGURE 3 : OPTIMAL LOAD OBTAINED BY MPPT ($R_{OPT-MPPT}$)COMPARED TO THE OPTIMAL DISCRETE LOAD ($R_{OPT-RES}$)

While emulating R_1 and R_2, the microcontroller is in a deep-sleep state and consumes only 2.5µA @1.8V. The voltage measurement is performed with a MOS commended voltage divider whose consumption is negligible over the whole system. The consumption of the 100kHz clock is of 4.5µA @ 1.8V which give an overall estimated consumption of 7µA @ 1.8V (12.6µW) when connected to an external power supply.

IV. Conclusion

This work shows the first results of a MPPT algorithm that applies a two-measurements method on a weakly coupled PEH while consuming only 7 µA (@1.8V). The system continuously harvests energy and wakes up each time it changes from a measurement phase to a sleep phase where the optimal load is emulated. A next step would be to test this algorithm with a more coupled PEH so the impact of the load variation can be seen in more detail. It will also be used as the sub-block of a more complex system, addressing highly coupled energy harvesters.

References

[1] S. Boisseau, P. Gasnier, M. Gallardo, and G. Despesse, "Self-starting power management circuits for piezoelectric and electret-based electrostatic mechanical energy harvesters," Journal of Physics, p. 6, 2013.

[2] N. Kong and D. S. Ha, "Low-Power Design of a Self-powered Piezoelectric Energy Harvesting System With Maximum Power Point Tracking," IEEE Transactions on Power Electronics, vol. 27, no. 5, pp. 2298–2308, May 2012, doi: 10.1109/TPEL.2011.2172960.

[3] B. Çiftci, S. Chamanian, A. Koyuncuoğlu, A. Muhtaroğlu, and H. Külah, "A Low-Profile Autonomous Interface Circuit for Piezoelectric Micro-Power Generators," IEEE Transactions on Circuits and Systems I: Regular Papers, pp. 1–14, 2021, doi: 10.1109/TCSI.2021.3053503.

[4] A. Brenes, A. Morel, J. Juillard, E. Lefeuvre, and A. Badel, "Maximum power point of piezoelectric energy harvesters: a review of optimality condition for electrical tuning," Smart Mater. Struct., vol. 29, no. 3, p. 033001, Mar. 2020, doi: 10.1088/1361-665X/ab6484.

[5] O. Freychet et al., "Efficient optimal load and maximum output power determination for linear vibration energy harvesters with a two-measurement characterization method," Smart Mater. Struct., vol. 29, no. 1, p. 015003, Jan. 2020, doi: 10.1088/1361-665X/ab516f.

[6] N. Decroix, P. Gasnier, and A. Badel, "An Efficient Maximum Power Point Tracking Architecture for Weakly Coupled Piezoelectric Harvesters based on the source I–V curve," in 2021 IEEE 20th International Conference on Micro and Nanotechnology for Power Generation and Energy Conversion Applications (PowerMEMS), Dec. 2021, pp. 136–139. doi: 10.1109/PowerMEMS54003.2021.9658370.

A wideband piezoelectric vibration energy harvester

Nabil BENCHEIKH[1,*], Timotéo PAYRE[1], Alexandre PAGES[1], Aya BENHAMOU[2] Adrien BADEL[2]

[1] *Cedrat Technologies, 59 Chemin du Vieux Chêne, 38240 Meylan*

[2] *USMB SYMME, 5 chemin de Bellevue ANNECY-LE-VIEUX, CS 80439, 74944 ANNECY-LE-VIEUX CEDEX*

**Corresponding author: nabil.bencheikh@cedrat-tec.com*

***Abstract* — This paper focuses on the design of the bistable energy harvester based on a patented solution invented by the SYMME / USMB laboratory and using Amplified Piezoelectric Actuator (APA®) technology. A preliminary prototype is developed considering the lifetime and mechanical limitations. Experimental results are also given for swept sine and random vibration.**

I. INTRODUCTION

The development of embedded and autonomous sensing solution is increasing in several industrial applications. The major constraints for the development of such devices is the availability of energy/power supply. Especially for applications implying a high cost for maintaining the function such as transport network (over cities, countries…). For these applications, solutions based on batteries have a lifetime limitation and wires supply are not adapted due to the accessibility and difficulty of installation.

The development of energy harvester solutions is increasing in the same way with the autonomous senor. Several solutions are already available on the market and on laboratories.

The most answered solution uses a linear oscillator tuned to match the excitation vibration. The narrow band solutions exploit a high mechanical quality factor at the frequency resonance of the linear oscillator. Contrariwise, these solutions are sensitive to any variation of the excitation vibration. On other hand, the environmental excitations have an energy dispersed over a frequency spectrum. A large bandwidth harvesting solutions are in this case required.

As a solution, bistable oscillators were proposed in the literature for energy harvesting as they offer a large bandwidth behaviour. Bistability is usually obtained thanks to either magnetic attraction/repulsion [1], either buckling effect [2]. This paper proposes a solution based on mechanical buckling effect.

II. EXCITATION SIGNAL

The preliminary design of any energy harvester requires an analysis of the excitation vibration signals and to know dispersion of the energy according to the vibration records. The performed analysis allow to have the mean representative signal. The mean signal shows an acceleration level of 3.5 g and two frequencies 110 and 180 Hz.

III. THE BISTABLE REPRESENTATION

A. The modeling

For the modeling, the architecture of the bistable energy harvester is simplified as given hereafter (FIGURE 1).

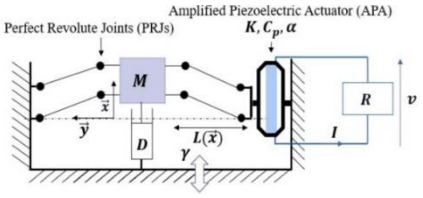

FIGURE 1. BISTABLE REPRESENTATION

The equation of motion and the current expression are provided in (1) from [2, 3]. K, C_p and α are the stiffness, the capacitance and coupling constant of APA respectively. The APA120 S was considered for this study. M, D and R are the equivalent mass, the damping coefficient, and the resistive load restive load respectively. γ is the base acceleration, x is the proof mass displacement and L is the beams length. x_0 is the buckling level and corresponds to the equilibrium position.

$$\begin{cases} M\gamma = M\ddot{x} - 2K\frac{x_0^2}{L^2}x + 2\frac{K}{L^2}x^3 + D\dot{x} + \frac{2\alpha}{L}xv \\ i = \frac{2\alpha}{L}x\dot{x} - C_p\dot{v} \end{cases} \quad (1)$$

B. The bistable response

The bistable response in terms of power and displacement was computed (the mean signal § II). Various values of M, L and $x_0$were tested. In order maximize the harvested power while considering boundaries such as volume limitations and preliminary feasibility criterions (e.g., minimal x_0 physically feasible). As an illustration, the Figure 2 represents the expected power as a function of x_0 and M for L =35 mm. The red points correspond to the realizable configurations.

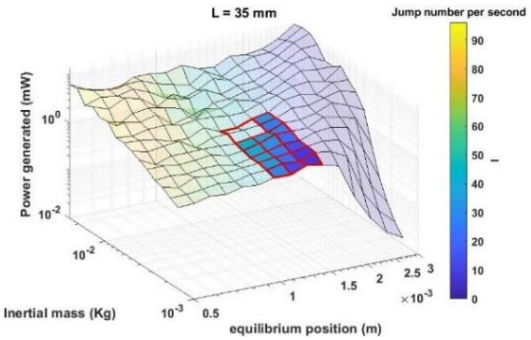

FIGURE 2. EXPECTED POWER AND JUMP BETWEEN THE EQUILIBRIUM POSITIONS AS REPONSE

The dimensional parameter of the optimal design corresponds to $L = 35\ mm$, $M = 5\ g$ and $x_0 = 0.85\ mm$.

IV. MECHANICAL DESIGN

A. *The amplified piezoelectric actuator constraint*

The APA® consist of piezoelectric material installed inside a metallic shell for an amplification and preload purpose. Two limitations are considered: the dismounting of the piezoelectric material and the stress on the metallic shell. These limitations imposed a displacement limitation at 50 µm in compression and 480 µm in tensile.

B. *The beam thickness*

The beam width was fixed at 10 mm. The beam thickness had to be selected considering the limitations as it has a strong influence. The thickness must be limited to around 400 µm and 350 µm to not exceed the yield stress and APA® compression limits respectively. A thickness of 200 µm was considered for our prototype which correspond to 50 %of the yield stress.

V. PROTOTYPING AND EXPERIMENTS

A. *Prototyping*

The prototype is design and manufactured (FIGURE 3) according the optimal design (§ 0). The prototype allows the integration of different size of APA®.

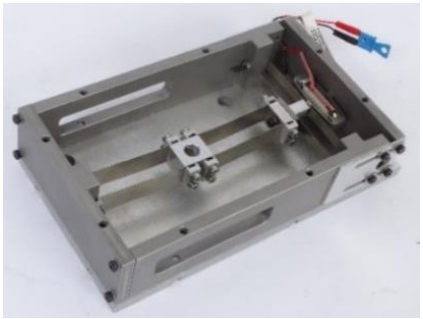

FIGURE 3. PROTOTYPE OF BISTABLE ENERGY HARVESTER

B. *Experimentation*

1) *Swept sine vibration*

The first evaluation is performed upon resistive load set at 1500 Ohm. The excitation vibration corresponds to swept sine vibration from 35 to 175 Hz at 3.5 g acceleration.

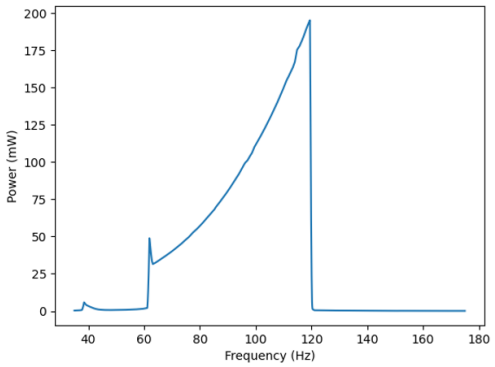

FIGURE 4. THE EXTRACTED POWER ON THE RESISTIVE LOAD

The minimum dissipated power upon the resistive load is about 30 mW at frequency 90 Hz ± 60% (Figure 4). The power raises the 190 mW at 120 Hz.

2) *Random vibration*

In random vibration test campaign, two profiles of vibration are used. The first profile (PSD1) includes two peaks at 110 and 178 Hz. The second profile (PSD2) include only one peak at 110 Hz. The comparison between two profile is given below (Figure 5).

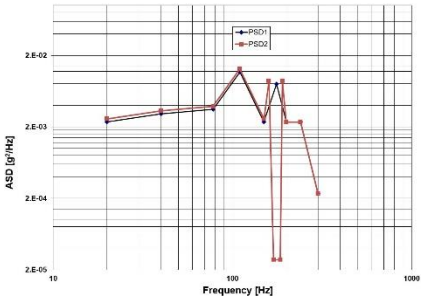

FIGURE 5. THE PROFILE OF PSD1 AND PSD2 VIBRATION

The power / energy extracted from the bistable energy harvester are measured (Figure 6). The level of acceleration is 3 grms and the duration is about 3 minutes.

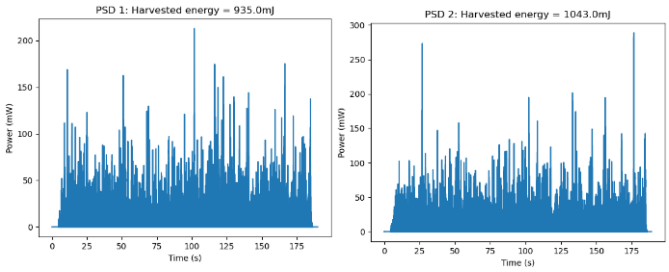

FIGURE 6. POWER / ENERGY EXTRACTED FROM BISTABLE HARVESTER WITH PSD1 AND PSD2 VIBRATION

The measurement shows a stability of the extracted energy even if there is a variation of the excitation signal.

VI. CONCLUSION

The broadband piezoelectric harvester has been presented in this document. The preliminary results show an available power of 30 mW at frequency 90 Hz ± 60% and 3.5 g acceleration. The random vibration test demonstrates a low sensitivity of the bistable energy harvester to two different PSD.

ACKNOWLEDGMENT

The RAILMON project has received funding from French financing and business development organization (BPI) through Support for the structuring research and development project for competitiveness programme (N° DOS1670841/00)

REFERENCES

[1] S. C. Stanton, C. C. McGehee, et B. P. Mann, « Nonlinear dynamics for broadband energy harvesting: Investigation of a bistable piezoelectric inertial generator », Physica D: Nonlinear Phenomena, vol. 239, no 10, Art. no 10, mai 2010, doi: 10.1016/j.physd.2010.01.019.

[2] T. Huguet, A. Badel, et M. Lallart, « Parametric analysis for optimized piezoelectric bistable vibration energy harvesters », *Smart Mater. Struct.*, vol. 28, n° 11, Art. n° 11, oct. 2019, doi: 10.1088/1361-665X/ab45c6

[3] W. Liu, A. Badel, F. Formosa, Y. Wu, N. Bencheikh and A. Agbossou. "*A wideband integrated piezoelectric bistable generator: Experimental performance evaluation and potential for real environmental vibrations*" *Journal of Intelligent Material Systems and Structures*, pp. 97-101, 2014.

An Information Theory Approach to Vibration Energy Harvesting

Francisco AMBIA[1,*] and Elie LEFEUVRE[1]

[1] Centre de Nanosciences et de Nanotechnologies, 10 Boulevard Thomas Gobert 91120 Palaiseau

*jose-francisco.ambia-campos@universite-paris-saclay.fr

***Abstract*—Understanding the limits of output power for an arbitrary excitation force or acceleration allows us to assess the effectiveness of energy harvesting systems. We propose a simple information measurement that quantifies how close an energy harvester is to the fundamental limits of performances. The proposed technique is implemented experimentally on an electrostatic MEMS to assess its efficiency though time.**

I. Introduction

An important constraint in vibration energy harvesting devices is the limit of displacement that the inertial mass is allowed to do. This displacement constraint may come from the yield strength of deformable elements, or simply the limited available space for a given application. Optimal trajectories for periodic excitations with displacement constraints were derived in [1]. In this paper, the authors derive a power bound that cannot be circumvented by any transducer or electronic interface. Another study for arbitrary accelerations was done in [2], in which an optimal energy harvesting strategy called "buy-low-sell-high" (BLSH) was proposed. A displacement constraint was considered to derive the optimal trajectory for an irregular broadband low-frequency excitation.

Based on the BLSH strategy, we propose a coarse-grained approximation of an arbitrary vibration energy harvester. An analogy is made between a binary communication channel and the coarse-grained harvester model. It is shown that the capacity of the communication channel is related to the effectiveness of the energy harvester.

II. BLSH and Mutual Information

The BLSH strategy [2],[3] maximizes the average input mechanical power $\langle P_{in}\rangle = \int_0^{t_f} F(t)\dot{u}(t)dt\,/t_f$ where $F(t)$ is the driving external force and $u(t)$ is the position of the mass. Integrating by parts and considering long times t_f we obtain an expression in terms of $\dot{F}(t)$ and $u(t)$.

$$\langle P_{in}\rangle = -\frac{1}{t_f}\int_0^{t_f} u(t)\,\dot{F}(t)dt \tag{1}$$

The BLSH strategy maximizes the mechanical input power given in Eq. (1) by controlling the mass position under the displacement constraint $-u_{max} \le u(t) \le u_{max}$. To maximize the average power in Eq. (1), firstly we chose the sign of $u(t)$ so that we always integrate positive values of $-u(t)\dot{F}(t)$, secondly we choose extreme values of $u(t)$ either u_{max} or $-u_{max}$, these two criteria maximize the integral in Eq. (1) and define the ideal harvesting trajectory under displacements constraints. The ideal trajectory discussed above is described by Eq. (2).

A slight change was done on Eq. (2), instead of using the excitation force $F(t)$ as in [2], the acceleration $a(t) = F(t)/m$ was used for the sake of generality.

$$u_{BLSH}(t) = -u_{max}sgn\big(\dot{a}(t)\big) \tag{2}$$

A. Coarse-grained approximation

The position and the driving acceleration are continuous-time real valued signals, in the course grained approximation they are considered as discrete-time binary signals.

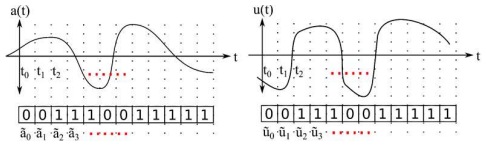

FIGURE 1. Coarse-grained approximation for position and acceleration signals

Time is discretized in steps of duration Δt, being time $t = i\Delta t$, where i is an integer. The acceleration is considered bandwidth limited, $\hat{a}(f > f_{max}) = 0$ with $2f_{max} < 1/\Delta t$ so we are able to capture all the details of the waveform according to the Nyquist-Shannon sampling theorem. Let us define the binary variable $\tilde{a}_i$ that takes value of 0 when $\dot{a}(i\Delta t) \ge 0$ and 1 when $\dot{a}(i\Delta t) < 0$. For the position, we define $\tilde{u}_i$ that takes 0 value when $u(i\Delta t) \le 0$ and 1 when $u(i\Delta t) > 0$. The criteria described above is illustrated in FIGURE 1.

When the two chains of bits $\tilde{a}_i$ and $\tilde{u}_i$ are the same, the coarse grained approximation is compliant with the protocol described in Eq. (2) and the ideal displacement waveforms in Ref. [1] [2]. Moreover, note that when a linear oscillator is in resonance and we apply the approximation described above, we get identical bit chains for $\tilde{a}_i$ and $\tilde{u}_i$.

B. Binary Communication Channel

Consider a binary communication channel as the one depicted in FIGURE 2, in such system the output $\tilde{u}_i$ depends probabilistically on its input $\tilde{a}_i$ [4]. For each input, there is a probability of communication error, for instance the probability of having 1 as input and getting 0 in the output. According to Shannon's Theorem the ultimate limit on the rate of communication over a channel is given by its capacity. The channel capacity is related to the mutual information $I(\tilde{a};\tilde{u})$. Mutual information is a measure of the amount of information

that one random variable $\tilde{u}$ contains about other random variable $\tilde{a}$.

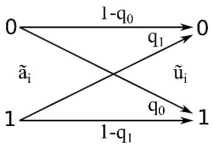

FIGURE 2. BINARY COMMUNICATION CHANNEL

Mutual information depends in the marginal entropies of the input and output and their joint entropy as:

$$I(\tilde{a};\tilde{u}) = H(\tilde{a}) + H(\tilde{u}) - H(\tilde{a},\tilde{u}) \quad (3)$$

Entropy H is the average amount of information that one needs to describe a random variable. If one needs less information to describe two random variables together than separately, it means that the two variables are to some degree redundant. $I(\tilde{a};\tilde{u})$ measures the information that $\tilde{u}$ and $\tilde{a}$ share.

III. VIBRATION ENERGY HARVESTER AS A COMMUNIACTION CHANNEL

The coarse-grained approximation described in II.A allows to consider the harvester as a communication channel. Each element in the bit chain $\tilde{a}_i$ will be transmitted to $\tilde{u}_i$ with some probability of transmission error, the higher the error rates q_0 and q_1, the less information that $\tilde{u}$ and $\tilde{a}$ share and the lower mutual information $I(\tilde{a};\tilde{u})$ will be. An error of information transmission is also failing to follow the BLSH protocol (2).

The mutual information can be obtained by calculating a normalized histogram taking the bit chains $\tilde{a}_i$ and $\tilde{u}_i$. The histogram consist on four relative frequencies: $q_{00}, q_{10}, q_{01}, q_{11}$. The first bit in this notation corresponds to $\tilde{a}$ and the second to $\tilde{u}$. For instance, relative frequency q_{10} is the ratio of the number of occurrences of having 1 as input $\tilde{a} = 1$ and getting 0 as output $\tilde{u} = 0$ divided by the total number of bits in the chain.

A. *Effectiveness*

The protocol of Eq. (2) maximizes the input mechanical power that goes into the system, this gives the maximal harvesting opportunity to the harvester's transducer.

One can define effectiveness ε as the ratio of power that goes into the system over the maximum power available in the acceleration signal [2].

$$\varepsilon = \frac{\int_0^{t_f} a(t)\,\dot{u}(t)dt}{u_{max}\int_0^{t_f}|\dot{a}(t)|\,dt} \quad (4)$$

B. *MEMS Mutual information and effectiveness*

MEMS devices have displacement constraints, this makes valid the assumptions in section II. A device intended for biomedical implants similar to the one presented in [5] was used to test the information and effectiveness measurements. The device was subject to a recorded acceleration of a human chest downloaded via The EH Network Data Repository. The acceleration signal has three excitation levels acceleration: a volunteer slow walking, normal walk and finally jogging.

We calculate the mutual information and effectiveness according to equations (3) and (4) respectively. The obtained signals of mutual information and effectiveness have the same tendencies, although they show a time delay, they have the same dependence on the acceleration signal as shown in FIGURE 3.

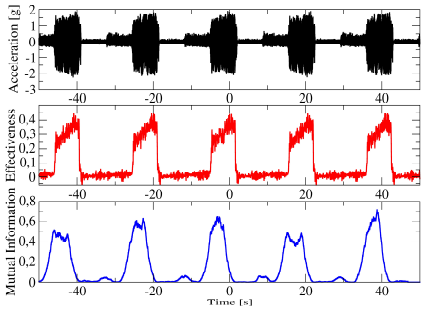

FIGURE 3. ACCELERAION, EFFECTIVENESS AND MUTUAL INFORMATION OF A MEMS DEVICE UNDER RECORDED HUMAN ACCELERATIONS

Mutual Information is an indicator of how close an energy harvester is to the fundamental limit [2]. For example, in the case where one has control the spring constant of a linear oscillator under harmonic accelerations of unknown frequency, one can search for the most adequate spring constant by finding the spring constant where the Mutual Information is maximum.

IV. CONCLUSION

We have demonstrated that the mutual information and effectiveness have similar behaviors, these results could pave the way to use the approach presented to consider mutual information as a cost function to optimize vibration energy harvesters. The low energy cost of calculating the mutual information is interesting for energy harvesting applications: There is no need of ADC for acquiring signals because are $\tilde{u}$ and $\tilde{a}$ binary, is a minimalistic computation, needing four digital counters. Most importantly the approach makes no assumption on the dynamics of the system making it useful for a wide range of harvester transduction mechanisms and circuit interfaces.

ACKNOWLEDGMENT

This work received support from the cleanroom facility of the Centre For Nanoscience and Nanotechnology, and the French RENATECH nanofabrication network.

REFERENCES

[1] E. Halvorsen, C. P. Le, P. D. Mitcheson, and E. M. Yeatman, "Architecture-independent power bound for vibration energy harvesters," in *Journal of Physics: Conference Series*, 2013, vol. 476, no. 1, p. 012026.

[2] A. H. Hosseinloo and K. Turitsyn, "Fundamental limits to nonlinear energy harvesting," *Phys. Rev. Appl.*, vol. 4, no. 6, p. 064009, 2015.

[3] A. Karami, J. Juillard, E. Blokhina, P. Basset, and D. Galayko, "Electrostatic Near-Limits Kinetic Energy Harvesting from Arbitrary Input Vibrations," *ArXiv Prepr. ArXiv200207086*, 2019.

[4] T. M. Cover and J. A. Thomas, *Elements of Information Theory*. John Wiley & Sons, 2012.

[5] F. Ambia, J. Chavez, M. Lallart, X. Leroux, and E. Lefeuvre, "Design and Simulation of an Electrostatic Energy Harvester for Biomedical Implants," in *2021 Symposium on Design, Test, Integration & Packaging of MEMS and MOEMS (DTIP)*, 2021, pp. 1–6.

Benefits of the collective dynamics for efficient broadband energy harvesting

Kaouthar AOUALI*, Shakiba DOWLATI, Najib KACEM and Noureddine BOUHADDI
Univ. Bourgogne Franche-Comté, FEMTO-ST Institute, CNRS/UFC/ENSMM/
UTBM, Department of Applied Mechanics, 25000 Besançon, France
*kaouthar.aouali@femto-st.fr

***Abstract*— The functionalization of internal resonance (IR) is theoretically and experimentally demonstrated on a nonlinear hybrid piezoelectric (PE)-electromagnetic (EM) vibration energy harvester (HVEH). This nonlinear phenomenon is tuned by adjusting the gaps between the moving magnets of the structure, enabling 1:1 and 2:1 IR. The experimental results prove that the activation of 2:1 IR with a realistic basis excitation amplitude (0.7 g) allows the improvement of both the frequency bandwidth (BW) and the harvested power (HP) by 300 % and 100 %, respectively compared to the case away from IR.**

I. INTRODUCTION

Over the last decades, converting ambient vibration energy into electricity to run low-power wireless electronics has received growing interest [1]. Generally, most vibration harvesters operate at a certain frequency. However, the narrow frequency range of the resonators limits their harvesting efficiency when the environment excitation frequency doesn't match the harvester natural frequency.

To avoid this critical issue, several researchers have attempted different methods to extend the frequency bandwidth of the harvesters [2,3]. Among these methods, the internal resonance is investigated [4]. This nonlinear phenomenon occurs in multiple degree-of-freedom (DOFs) systems and results in a broader bandwidth. This phenomenon is characterized by a double-jumping in the frequency response which bends to the left and to the right simultaneously from the central frequency [5, 6]. It occurs when the natural frequencies of the multiple DOFs system are tuned so that they are commensurable.

This paper investigates the activation and tuning of the IR phenomenon by adjusting the structure magnets' gaps. It is shown that the functionalization of the 2:1 IR allows a significant improvement of the frequency bandwidth and the harvested energy simultaneously over the case away from IR.

II. MODEL AND EXPERIMENTAL SETUP

The designed HVEH integrating simultaneously PE-EM conversion mechanisms is depicted in FIGURE 1a. It includes two piezoelectric layers attached on the top surface of each beam near the clamped ends. It consists of two center movable coupled magnets supported by the compound elastic beams. The coupling between the magnets is tuned by varying the gaps using the threaded rigid bars. A wire-wound copper coil is placed around each moving magnet. Applying a harmonic base excitation, the magnets oscillate around their equilibrium positions and the piezoelectric plates are subjected to mechanical stress. Therefore, EM and PE elements generate output powers based on Lorentz's Law and direct piezoelectric effect, respectively.

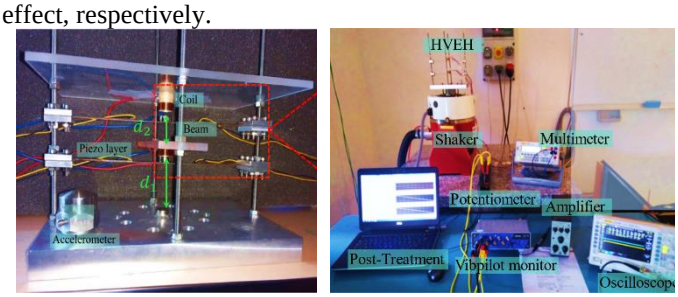

a) b)

FIGURE 1. A) THE PROPOSED HYBRID ENERGY HARVESTER B) THE EXPERIMENTAL SETUP

Considering x_i as the vibration amplitude of the magnet i (i = 1,2) and by expanding the magnetic force in Taylor series up to the third order, the equations of motion of the system can be written as follows:

$$\begin{cases} \ddot{x}_1 + 2\,\omega_0\,\xi\,\dot{x}_1 + \omega_0^2\,[(1+\beta_1+\beta_2)x_1 - \beta_2 x_2] + f^1_{mg,1}x_1^2 - \\ f^1_{mg,2}(x_2-x_1)^2 + f^1_{mg,3}x_1^3 - f^1_{mg,4}(x_2-x_1)^3 - \theta_1\,V_p^1(t) = -\ddot{Y} \\ \ddot{x}_2 + 2\,\omega_0\,\xi\,\dot{x}_2 + \omega_0^2\,[(1+\beta_2)x_2 - \beta_2 x_1] + f^2_{mg,1}(x_2-x_1)^2 + \\ f^2_{mg,2}(x_2-x_1)^3 - \theta_2 V_p^2(t) = -\ddot{Y} \end{cases} \quad (1)$$

where ξ is the damping factor, ω_0 is the eigenfrequency of the decoupled DOF, β_1 and β_2 are the coupling coefficients related to the top and bottom magnets, V_p^i is the output voltage of the i^{th} PE element, θ_i is the i^{th} PE element transfer factor, $\ddot{Y}$ is the acceleration of the basis excitation and $f^i_{mg,i}$ are nonlinear terms derived from the magnetic force.

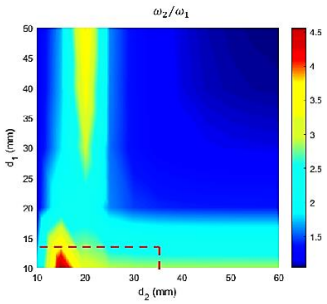

FIGURE 2. RATIO OF THE NATURAL FREQUENCY ω_2 TO ω_1 WHILE VARYING THE GAPS D_1 AND D_2

The linear natural frequencies ω_1 and ω_2 of the 2-DOFs harvester for undamped free vibrations are such that:

$$\omega_{1,2} = \omega_0 \frac{\sqrt{2(1+\beta_1)+\beta_2 \pm \sqrt{4\beta_1^2+\beta_2^2}}}{\sqrt{2}} \quad (2)$$

By changing the separation distances d_1 and d_2, we modify the coupling values. These gaps can be adjusted so that a modal interaction of 2:1 ratio is achieved and thus 2:1 internal resonance occurs. Setting $d_2^* = 35$ mm, the required distance d_1^*, satisfying that the second modal frequency of the structure is nearly twice its first modal frequency, is equal to 12.74 mm. Experimental findings have been performed. To do that, the experimental test bench was set as shown in FIGURE 1b. The power of nonlinear energy harvesting is evaluated according to $P = {V^2}/{R_{load}}$ for different load resistance at the base excitation level of 0.7 g where R_{load} is either R_{pe} or R_{em} according to the conversion mechanism. Throughout the experiments, the voltage frequency responses are recorded in terms of the root mean-square (RMS) value.

III. Results and Discussion

A basis acceleration of 0.7 g is applied. Up and down sweeps are done during the experiments to capture the bifurcation points of the nonlinear frequency response. For the optimal load resistances that maximize the harvested PE and EM powers, and for the well-chosen gaps values, experimental tests have been performed to determine the nonlinear dynamic behavior of the hybrid harvester.

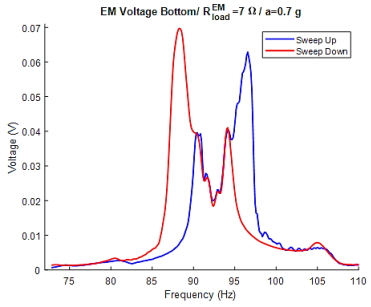

a)

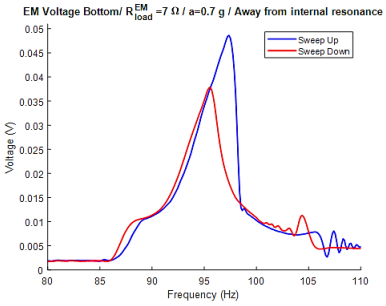

b)

FIGURE 3. A) FREQUENCY RESPONSE WITH OPTIMAL PARAMETERS ENSURING THE ACTIVATION OF THE INTERNAL RESONANCE PHENOMENON B) FREQUENCY RESPONSE AWAY FROM INTERNAL RESONANCE CONDITION AROUND THE 1ST RESONANCE FREQUENCY

Under these conditions, the second natural frequency ω_2 is of 185 Hz and is equal to twice the first natural one $\omega_1 = 92.5$ Hz according to Eq. (2). Through experiments, it has been shown that for $\omega_2 = 175.5$ Hz giving a ratio $\omega_2/\omega_1 = 1.9$, the internal resonance phenomenon is activated. In fact, the response curves show the existence of an additional peak that appears around the frequency of the first mode of the bottom DOF where hardening and softening responses are simultaneously observed as shown in FIGURE 3a. These results clearly demonstrate the modal interaction and energy transfer between the first and second modes that occurred because of the designed proportional relationship of natural frequencies.

To highlight the importance of the internal resonance phenomenon toward the output performance of the harvester, a configuration away from internal resonance is studied. The distances d_1 and d_2 are fixed both to 50 mm such that $\omega_1 = \omega_2$. FIGURE 3b shows the output voltage of the hybrid energy harvester away from the 2:1 internal resonance condition. Only softening nonlinearity is demonstrated. It is observed that the activation of the internal resonance results in increasing both the power density and the frequency bandwidth. An enhancement of 100% of power density is achieved compared to the generator away from the 2:1 internal resonance. By defining the internal resonance frequency bandwidth as the two upward peaks on both sides of the downward peak, it is also shown that the internal resonance widens the frequency bandwidth by 300% comparing to the case away from 2:1 internal resonance.

IV. Conclusion

The functionalization and the tuning of the phenomenon of internal resonance to enhance the performance of a nonlinear hybrid piezoelectric-electromagnetic harvester are demonstrated in this paper. By adjusting the gaps between the magnets, the natural frequencies of the harvester are tuned so that they are commensurate. Experiments capture the nonlinear behavior of the internal resonance phenomenon. In fact, the existence of two peaks around the first and the second primary resonance results in a wider bandwidth and a larger output. It has been also demonstrated that for well-chosen gaps resulting in 2:1 IR, an enhancement of 100 % increase in the harvested power and an enlargement of 300 % in the bandwidth are achieved.

References

[1] Roundy, Shad, and Paul K. Wright. ”A piezoelectric vibration based generator for wireless electronics.” Smart Materials and structures 13.5 (2004): 1131

[2] Tang, Lihua, Yaowen Yang, and Chee Kiong Soh. ”Toward broadband vibration-based energy harvesting.” Journal of intelligent material systems and structures 21.18 (2010): 1867-1897.

[3] Zhu, Dibin, Michael J. Tudor, and Stephen P. Beeby. ”Strategies for increasing the operating frequency range of vibration energy harvesters: a review.” Measurement Science and Technology 21.2 (2009): 022001.

[4] Jiang, Wen-An, et al. ”Broadband energy harvesting based on one-to-one internal resonance.” Chinese Physics B 29.10 (2020): 100503.

[5] Xiong, Liuyang, Lihua Tang, and Brian R. Mace. ”Internal resonance with commensurability induced by an auxiliary oscillator for broadband energy harvesting.” Applied Physics Letters 108.20 (2016): 203901.

[6] Nie, Xiaochun, et al. ”Broadband and high-efficient L-shaped piezoelectric energy harvester based on internal resonance.” International Journal of Mechanical Sciences 159 (2019): 287-305.

Design of a piezoelectric transducer for strain energy harvesting in automotive application

Arthur GIVOIS [1,2,*], Florian ALLEIN[1] , Charles CROËNNE[1] , Hung LE KHANH[2], Hervé DIETSCH[2] and Bertrand DUBUS[1]

[1] *Univ. Lille, CNRS, Centrale Lille, Univ. Polytechnique Hauts-de-France, Junia, UMR 8520 - IEMN, F-59000 Lille, France*

[2] *Michelin Recherche et Technique SA, Givisiez, Switzerland*

*arthur.givois@junia.com

***Abstract*— We investigate the power harvesting capability of the strain energy in a wheel, generated by the contact with pavement at each wheel cycle. In a first step the energy dissipated in a resistor is simulated for different geometric configurations of composite piezoelectric transducers, made of parallelepipedic PZT cubes embedded in a polymer matrix. We notice that the mechanical coupling between matrix and transducer materials plays a key role in the efficiency of the energy harvesting set-up. We find that at the composite level, the estimated maximal converted energy is highly sensitive to the physical nature of the mechanical load. A second part of this work, currently in progress, is devoted to the characterization of the mechanical load and the link between the whole wheel structure and the composite scale.**

I INTRODUCTION

The increase in requirements of the security standards in automotive industry has lead to the design of energy-consuming devices, which suffer from a lack of autonomy for signal processing and communication operations. To address this issue, the implementation of mechanical energy harvesting devices in the wheel is a promising concept which has been the subject of various proposals in an industrial context over the last two decades [1-3].

In this framework, the choice of the transducer, the mechanical coupling of this latter to the host structure and the electric matching strategy in view of energy storage are of prime importance in view of efficient transduction and energy harvesting. Although a wide range of existing transduction solutions are regularly listed in the literature [4], the more recent reviews attest that no consensual strategy has emerged for this application [5-6], thus preventing from a robust and commercialized technology to be proposed. Among all these transduction technologies, the advantage of piezoelectric composites relies on the different possible geometric configurations of the piezoelectric element, respective to the one of the passive material, which offers flexibility in the design of the transducer in view of its adaptation to the host structure [7]. The few configurations tested underlined the potential of this type of transducer [8], without definitive proof concerning the generation of sufficient power for reaching the autonomy of monitoring systems in vehicles.

In particular, no detailed investigation of an optimal transducer configuration, discussing the geometric configuration of the composite, the material properties of the surrounding matrix and the placement in the wheel, was proposed to our knowledge. This study aims at evaluating the maximum recoverable energy in a piezoelectric composite transducer embedded in a wheel of an automotive equipment. In the design procedure, we focus on the mechanical coupling between the host structure and the piezoelectric sensor.

II COMPOSITE SIMULATION FRAMEWORK

II.A Modeling of the piezoelectric composites

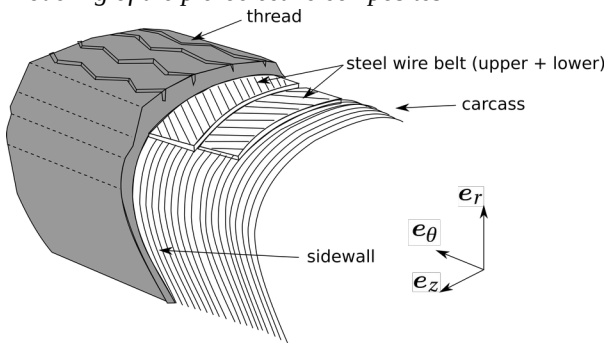

FIGURE 1. REPRESENTATION OF THE CAR WHEEL (FROM [9]).

The host structure is in the form of a circular geometry, where the position of a material point is described in the cylindrical reference frame (e_r, e_θ, e_z). The geometry of a section in the azimuthal plane, depicted in Figure 1, is defined by a curve on which is placed a laminate comprising a carcass layer. The thread in the upper part comprises alternating polymer layers and two braided steel belts. The sidewalls on the lateral parts are composed of three layers, the carcass being surrounded by two polymer layers. To evaluate the performance of the inserted transducer, we model a network of composite cells as described in Fig. 2: a unit cell is modeled using the finite element method, and periodic boundary conditions are applied to the unit cell in order to consider a semi-infinite composite network.

FIGURE 2. SCHEMATIC OF THE COMPOSITE NETWORK INTRODUCED IN THE HOST STRUCTURE (A); GEOMETRIC CONFIGURATION OF A UNIT CELL (B); ELECTRIC SCHEME OF THE CONNECTION TO A RESISTANCE LOAD (C). GREY: POLYMER; ORANGE: MATRIX; BROWN: ELECTRODES; YELLOW: PIEZOELECTRIC ELEMENT.

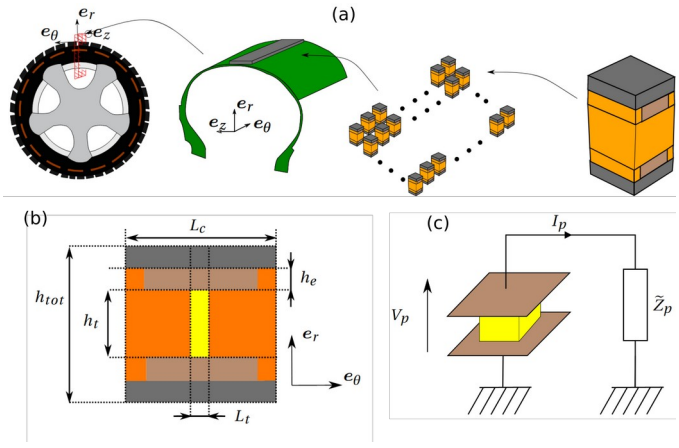

We finally obtain an estimation of the recoverable power at the resistance load, for a harmonic mechanical input whose frequency corresponds to a low vehicle speed (35 km/h). At this stage of the study, we tune the value of the resistance load to the

frequency of the mechanical input and to the geometric properties of the piezoelectric cell.

II.B Mechanical loads and varying composite parameters

For the simulations, the mechanical loads applied to the transducer are either stresses or strains. There are preliminary evaluated by simulating the whole rolling wheel without the transducer and by selecting a set of placements in the wheel for which we extract the values of stresses and strains. Table 1 gathers a selected set of tested configurations, in which letters A to F correspond to specific locations in the wheel. This approach relies on the assumption that the integration of the transducer does not affect significantly the mechanical energy density.

TABLE 1. LOCATIONS OF THE TRANSDUCER AND MECHANICAL VALUES (NOTATIONS I AND II REFER TO THE SCHEMATIC IN FIG. 1). STRESSES AND STRAINS ARE RESPECTIVELY DENOTED BY T AND ε.

Load configuration	Piezoelectric effect	Mechanical Load
A_T	33	$T_{rr}=100$ kPa
A_ε	33	$\varepsilon_{rr}=0.25$ %
B_T	13	$T_{\theta\theta}=100$ kPa
B_ε	13	$\varepsilon_{\theta\theta}=0.25$ %
C_T	15	$T_{r\theta}=120$ kPa
C_ε	15	$\varepsilon_{r\theta}=6$ %
D_T	13	$T_{\theta\theta}=25$ kPa
D_ε	13	$\varepsilon_{\theta\theta}=0.5$ %
E_T	13	$T_{\theta\theta}=100$ kPa
E_ε	13	$\varepsilon_{\theta\theta}=1.5$ %
F_T	15	$T_{r\theta}=180$ kPa
F_ε	15	$\varepsilon_{r\theta}=10$ %

We preliminary evaluate the dissipated power in the resistance when varying the material matrix properties and geometric configurations. These first evaluations show that:

- Maximal powers are obtained for maximal or minimal values of the input parameters of the composite transducer
- Matrix material should be as flexible and compressible as possible.

Consequently, we adopt a brute force approach, where each of the parameters is varied in pairs. The main varying parameters are the length, width, thickness of the composite, as well as the length and width of the cell relatively to the overall circumference of the wheel (cf. Fig. 2 (b)). At the end, the output recoverable powers are estimated for $2^5=32$ geometric parameter sets at each mechanical load case and an optimal composite configuration is determined.

III RESULTS OF ESTIMATED POWERS

Maximal dissipated powers for each load case are shown in Table 2. The best performances are obtained when the mechanical drive is a displacement, whereas low powers are systematically obtained when the drive is a stress. It is noticeable that the preferred geometric configurations of piezoelectric composites are in the form of micro-plates.

At the structural level, using a strain as a mechanical drive corresponds to a bending mechanism. Indeed, the kinematics of thin-walled structure is described by a continuous varying in-plane strain in the thickness. Further simulations of a whole wheel are conducted with and without a thin composite layer to evaluate in which extent the kinematics is modified by the integration of the composite.

Load Config.	A_T	B_T	C_T	D_T	E_T	F_T
Max. recov. power [mW]	0.203	0.023	0.257	0.001	0.017	0.54
C_p [nF]	3.10^{-6}	2.10^{-5}	0.014	0.124	0.124	0.015
Load Config.	A_ε	B_ε	C_ε	D_ε	E_ε	F_ε
Max. recov. power [mW]	0.111	115	495	445	3497	1368
C_p [nF]	3.10^{-6}	0.37	2.10^{-5}	0.37	0.37	0.015

TABLE 2. ESTIMATED POWERS DISSIPATED IN THE RESISTANCE LOAD AND CORRESPONDING CAPACITANCE OF THE UNIT PIEZOELECTRIC ELEMENT

FIGURE 3. GEOMETRIES OF THE UNIT CELL COMPOSITE CORRESPONDING TO

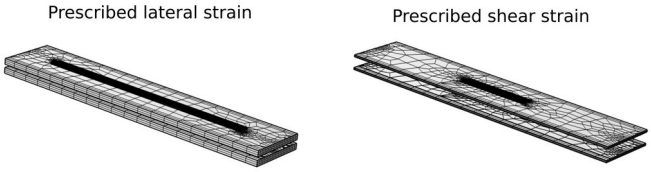

THE PREFERRED CONFIGURATIONS (E_ε AND F_εMECHANICAL LOAD IN TABLE 2). THE MATRIX MATERIAL IS MADE EMPTY.

IV CONCLUSION

We analyze the potential of energy harvesting in a wheel using piezoelectric transducers. To this end we perform simulations for a large set of inputs regarding the mechanical source of energy and geometric configurations of the composite. Considerations regarding the material properties of the matrix are also provided. This analysis should be supported by further simulations to identify the adequate choice for the mechanical energy source, and particularly to verify accurately that a bending mechanism is the main contribution of the strain energy.

REFERENCES

[1] S. Roundy, J. Bryzek, C. Ray, M. Malaga and D. L. Brown, "Power generation utilizing tire pressure changes." U.S. Patent 7,260,984, 2007.

[2] J. D. Adamson, and G. P. O'brien, "System and method for generating electric power from a rotating tire's mechanical energy." U.S. Patent No. 7,096,727. 2006.

[3] R. Martineau, "Flexible member energy conversion device", U.S. Patent No. 7508085, 2007.

[4] C. R. Bowen and M. H. Arafa. "Energy harvesting technologies for tire pressure monitoring systems", *Advanced Energy Materials*, vol. 5.7, p.1401787, 2015.

[5] M. Germer, U. Marschner and A. Richter, "Energy Harvesting for Tire Pressure Monitoring Systems from a Mechanical Energy Point of View." *IEEE Internet of Things Journal*, vol. 9, pp. , 2022.

[6] J. Lee and B. Choi. "Development of a piezoelectric energy harvesting system for implementing wireless sensors on the tires." *Energy conversion and management*, vol. 78, pp. 32-38, 2014.

[7] R. E. Newnham, D. P. Skinner, and L. E. Cross, "Connectivity and piezoelectric-pyroelectric composites." *Materials Research Bulletin*, vol. 13 (5), pp. 525-536, 1978.

[8] D. A. van den Ende, H. J. van de Wiel, W. A. Groen and S. van der Zwaag, "Direct strain energy harvesting in automobile tires using piezoelectric PZT–polymer composites", *Smart Mater. Struct.*, vol. 21, p. 015011, 2011.

[9] A. Todoroki, S. Miyatani, and Y. Shimamura. "Wireless strain monitoring using electrical capacitance change of tire: part I - with oscillating circuit", *Smart Mater. Struct.*, vol. 12 (3), p. 403, 2003.

Electrical characterization of PA-MBE grown GaN nanowires via conductive probe AFM - Effect of load and generator resistances

Tanbir Kaur SODHI[1,2*], Pascal CHRETIEN[2], Laurent TRAVERS[1], Frédéric HOUZE[2], Maria TCHERNYCHEVA[1] and Noelle GOGNEAU[1]

[1] *Centre de Nanosciences et de Nanotechnologies — CNRS – Université Paris-Saclay, UMR9001, 91120 Palaiseau, France*

[2] *Université Paris-Saclay, Centrale Supélec, CNRS, Laboratoire de Génie électrique et électronique de Paris, 91192 Gif-sur-Yvette, France - Sorbonne Université, CNRS, Laboratoire de Génie Electrique et Electronique de Paris, 75252, Paris, France*

*tanbir.sodhi@c2n.upsaclay.fr

I. Introduction

Novel energy harvesting solutions have been proposed in the past decade to develop self-powering micro/nano-electronic devices, hence eliminating their bulky components such as batteries. Promising candidates in this research field include energy harvesters based on piezoelectric nanowires (NWs). Due to their superior mechanical properties, exalted piezoelectric coefficients and sensitivity to small forces (nN-pN), NWs convert efficiently the ambient mechanical inputs into electrical energy. Hence, strong piezo-generation responses have been reported, with average output voltages ranging from several millivolts to 520 mV per GaN NW [1]. Furthermore, the integration of InGaN insertion in the GaN NWs volume has proven to improve the piezo-conversion capacity by 35% because of their exalted piezo-electric coefficients [2]. More recently, intrinsically p-doped GaN NWs have demonstrated an electro-mechanical conversion efficiency up to 43% [3]. Based on these promising piezoelectric responses, GaN NWs-based piezo-generators have demonstrated power densities in the μW-mW/cm^3 range [4]. Although the piezo-conversion capacity of the GaN NWs based active layer is important to optimize the piezo-generator performance, the measuring circuit used to harvest the piezo-generated energies is of equal importance. For the first time in the nanoscale regime, we investigate the influence of the load resistance of the electronics on the output voltage and the power generated by the NWs. We demonstrate that the internal impedance of the nanogenerator, which is the sum of the internal resistance of constituting nanowires, the contact resistance and the diode resistance, is non-negligible and strongly depends on the nanowire characteristics.

II. Manuscript

We study the piezoelectric response of an array of single vertically oriented PA-MBE grown GaN NWs via an atomic force microscope (AFM) equipped with a home-made modified Resiscope [5], which has been specifically adapted to perform piezo-conversion measurement on single nanowires. In our specific instrumental configuration, the conductive AFM tip, which is brought into contact with the surface under a controlled and constant normal force, scans over the array of vertically oriented NWs. Under the mechanical input of the AFM tip, and due to the piezoelectric properties of GaN, an electric field is created within the NW volume and an output voltage is generated. This output signal is simultaneously harvested through the conductive AFM tip, which forms a Schottky diode with the GaN [6].

This configuration allows an in-depth investigation of the parameters controlling the piezo-generation of the NWs, such as the applied force, the NW stiffness, the Schottky nano-contact or the surface charge effects [3]. Moreover, it also presents the advantage to reproduce the configuration similar to the nano-generator devices presenting a Schottky configuration (electrode harvesting the energies is directly in contact with the NWs). It is thus possible to establish a correlation between behaviors in play in single NWs and the devices.

The piezoelectric response of GaN NWs is controlled, in a first time, by their degree of deformation, itself strongly linked to the external mechanical input (applied force, type and frequency of deformation…) as well as the NW characteristics (dimensions, doping…). The electrode through which the piezo-generated energies are harvested also plays a crucial role in the harvester efficiency [3, 7]. However, there is another key function which may significantly impact the system's efficiency: the electronic circuit and especially the Load resistance (R_{load}).

Using our AFM-Resiscope configuration, we investigate the piezo-response of GaN NWs as a function of the R_{load} for different applied forces. Figure 1 presents the evolution of the output voltages as a function of the applied R_{load} values for 120 nN and 380 nN. We clearly demonstrate, for the first time in the nanoscale regime, that the piezo-electric response of the GaN NWs is influenced by the applied load resistance (R_{load}) of the electronics. This behavior appears in agreement with the ones reported in the literature for macroscopic harvester systems presenting a capacitor configuration [8].

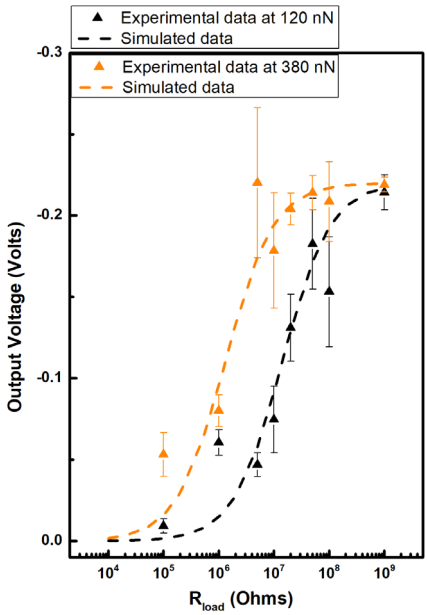

FIGURE 1. Influence of R_{load} on the piezo-generation capacity of non-intentionally n-doped GaN NWs for 120 nN and 380 nN of applied constant normal forces. The dashed lines have been simulated using least squares method as a visual indication of the output voltage evolution.

However, in our case, the active layer is a composite layer constituted by GaN NWs embedded in a soft matrix and contacted at their top via a Schottky diode. At this stage, one may wonder the influence of the NW resistance as well as the diode resistance on the piezo-generation.

In the nanogenerator research field, it is generally accepted that the resistance of the nanowires is negligible. Here, we demonstrate that the resistance of the nanogenerator, Rg, (in our configuration, it corresponds to the sum of contact resistance (Rc), Schottky diode resistance (R_S) and NW resistance (R_{NW})) has significant influence on the power generation capacity of the NWs. Especially we highlight its dynamic evolution as a function of the load resistance and applied constant normal force. Hence, we establish that to illustrate the influence of the charge resistance and then determine the optimal one regarding the energy system efficiency, the classical equation used to calculate the power ($P_i = V_i^2 / R_{load}$) is not suitable and the following one must be considered.

$$P_i = {V_i^2}/{R_{load} + R_g} \quad (1)$$

where V_i is the O.V. measured for the 'i' NW.

Finally, we demonstrate that the value of the nanogenerator resistance depends on the nanowire characteristics such as their doping or their stiffness.

III. Conclusion

We establish the crucial role of load and generator resistances in the optimization of the electronics for the piezo-electrical measurements of single NWs as already demonstrated at micro-scale.

This result, associated with the high-conversion efficiency of the Ga(In)N NWs, opens new perspectives to improve the electromechanical coupling properties of the GaN NW based nano-generators, a pre-requisite for technological transfer.

Acknowledgment

This work was supported by EU Horizon 2020 ERC project 'NanoHarvest' (Grant 639052), the French National Research Agency through the GANEX program (ANR-11-LABX-0014) and the Scenic project (ANR-20-CE09-0005) and by the Paris-Saclay University.

References

[1] T. K. Sodhi. P. Chrétien, F. Houzé and N. Gogneau (to be submitted).

[2] N. Jegenyes, M. Morassi, P. Chrétien, L. Travers, L. Lu, F.H. Julien, M. Tchernycheva, F. Houzé, N. Gogneau, "High piezoelectric conversion properties of axial InGaN/GaN nanowires", Nanomaterials, vol. 8, pp. 367, 2018.

[3] N.Gogneau, P. Chrétien, T. Sodhi, L. Couraud, L. Leroy, L. Travers, J-C. Harmand, F. H. Julien, M. Tchernycheva and F. Houzé, " Electromechanical conversion efficiency of GaN NWs: critical influence of the NW stiffness, the Schottky nano-contact and the surface charge effects", Nanoscale, vol. 14, pp. 4965-4976, 2022.

[4] N. Jamond, P. Chrétien, F. Houzé, L. Lu, L. Largeau, O. Maugain, L. Travers, J-C. Harmand, F. Glas and E. Lefeuvre, "Piezo-generator integrating a vertical array of GaN nanowires", Nanotechnology, vol. 27, pp. 325403, 2016.

[5] N.Gogneau, P. Chrétien, E. Galopin, S. Guilet, L. Travers, J-C. Harmand and F. Houzé, "GaN nanowires for piezoelectric generators", Phys. Status Solidi RRL, vol. 8, pp. 414-419, 2014.

[6] N. Gogneau, P. Chrétien, E. Galopin, S. Guilet, L. Travers, J-C. Harmand and F. Houzé, "Impact of the GaN nanowire polarity on energy harvesting'', Appl.Phys.Lett, vol.104, pp. 213105, 2014.

[7] N. Jamond, P. Chrétien, L. Gatilova, E. Galopin, L. Travers, J-C. Harmand, F. Glas, F. Houzé and N. Gogneau, "Energy harvesting efficiency in GaN nanowire-based nanogenerators: the critical influence of the Schottky nanocontact'', Nanoscale, vol. 9, pp. 4610-4619, 2017.

[8] M.A. Johar, A. Waseem, M.A. Hassan, I.V. Bagal, A. Abdullah, J-S. Ha and S-W. Ryu," Highly Durable Piezoelectric Nanogenerator by Heteroepitaxy of GaN Nanowires on Cu Foil for Enhanced Output Using Ambient Actuation Sources", Adv. Energy Mater., vol. 10, pp. 2002608, 2020.

External polarization source for dielectric elastomer generators : triboelectric generator

Simon-Emmanuel HAIM[1,2,*], Claire JEAN-MISTRAL[2] and Alain SYLVESTRE[1]

[1] Univ. Grenoble Alpes, CNRS, Grenoble INP, F38000 Grenoble, France

[2] Univ Lyon, INSA-Lyon, CNRS, UMR5259, F-69621, France

*E-mail : simon-emmanuel.haim@g2elab.grenoble-inp.fr

***Abstract*— For the past decade, triboelectricity has been widely studied to design triboelectric based energy harvesters. In this work, we have deepened the studies on triboelectric generator used in a sliding mode, designing a fully equipped test bench to deal with high impedance load and strong capacitive couplings. An electrical coupling with a more conventional dielectric elastomer generator will be implemented in order to polarize the latest and thus make it electrically autonomous.**

I. Introduction

In the coming years, wireless sensor used in IoT will be widely deployed in a huge range of applications, such as structural monitoring or remote healthcare. Harvesting energy directly from the ambient environment represents an effective way to power those sensors instead of conventional chemical batteries. Electrostatic harvesters are one way to convert mechanical energy into electrical one. In previous works, we developed soft Dielectric Elastomer Generators [1][2]: the principle of these DEGs is to exploit in an external circuit the electricity produced by a variation of capacitance induced by a mechanical deformation of the polymer. Developed DEGs are low cost, lightweight, can adapt complex shapes and can develop an energy density one hundred times higher than piezoelectric materials (1.7 J/g). Deformation of a sample of 5 cm length has been performed under 50% strain at 1Hz, leading to an experimental average output power of 33 µW on a 300 kΩ output charge.

Two ways of polarizing a DEG have already been explored: the use of an electret [1] and the use of a piezoelectric cell [2]. The disadvantage of the first solution is a high sensitivity to external environmental conditions, while the second one presents a high encumbrance. That is the reason why a new way of polarizing a DEG has been suggested: the use of a triboelectric generator.

Introduced by Wang and co-workers [1], triboelectric generators develop a high power density (5.3W/m^2), are light (density of few g/cm^3), inexpensive and compliant so they can be installed in a huge variety of places, or easily integrated into technical textile. Triboelectric generators also operate at very low frequencies (around Hz), as well as DEG, hence the idea of coupling those two technologies to create an electrically autonomous electrostatic generator

II. Experiments

A. Realization of a test bench

Although triboelectricity has been observed for a long time, the physical principle behind this is still poorly understood because many parameters are involved such as surface state, humidity, mechanical strains… The first step to study triboelectricity is the choice of material, based on triboelectric series, which are tables that quantify the amount and the polarity of the charge obtained by applying a tested material to a reference one. Then a test benched had to be designed in order to deal with the difficulties related to the measurement of electrostatic phenomena, such as high voltage (above 1kV), high internal impedance and high sensitivity to parasitic capacitance. Therefore, a test bench equipped with Trek electrostatic probes, a Keithley electrometer and a decade box from 1MΩ to nearly 2GΩ has been designed. Thanks to this over-equipped bench, we have monitored the transfer of electrical charges between couples of materials forming the TENG (copper, PET, PTFE.) over thousands of cycles in sliding mode.

B. Method and results

Some tests consisted of rubbing a sheet of PTFE (0.05*50*50 mm^3) against a sheet of copper of the same surface. Until now, most of the experiments were performed without load to have a better insight of the physical phenomenon. One of the main observations obtained so far is that the surface charge density might be not as homogeneous as it is mostly presented in the literature. Indeed, this consideration is very advantageous during the realization of simulation, but the aim of those simulations is the dimensioning of prototype.

The set-up is the following: a sheet of PTFE was rubbed against a piece of copper of the dimensions described above, but here the usual electrode placed on the PTFE, which is usually polarized through electrostatic induction by the triboelectric charges, is replaced by three copper bands perpendicular to the translation direction (FIGURE 1).

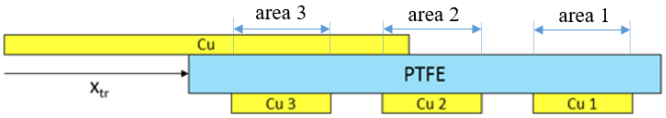

FIGURE 1. TENG with three electrodes

The potential of those three electrodes is then measured with electrostatic Trek voltmeters. These three electrodes provide a more accurate view of the triboelectric charge distribution than a single global electrode.

The simulation with Comsol uses the same geometric dimensions as the experiments, and a value of 1 µC/m^2 is used on the surface of the PTFE rubbed. As observed in FIGURE 2, the potential of the electrodes rise when the copper film passes them, but where the two differ is on the final value of the voltages: in the simulation, the three voltages tends to reach - 600V, whereas during the experiment the voltages reached are - 120V, - 150V and - 220V. The experiment result suggests that the more a part of the PTFE is rubbed, the higher its surface charge density is. Therefore, area 1 would be charged with 0.33 µC/m^2, while area 3 would only have 0.2 µC/m^2. This result is interesting for the dimensioning of a prototype, as it shows that to reach higher voltage, increasing the surface of the prototype is not enough, it becomes more interesting to increase the translation stroke of the device rather than its width. Some aspect still need to be considered in this study, like the homogeneity of the pressure between the sheets of copper and of PTFE.

a)

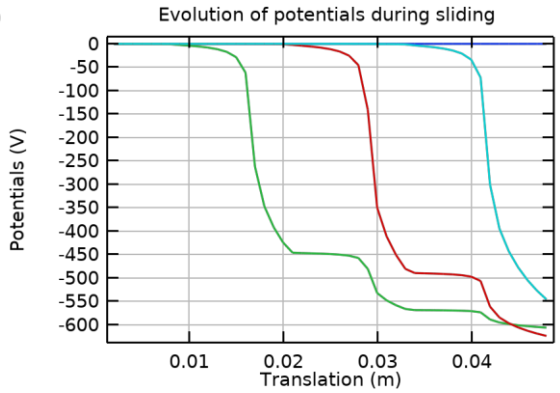

b)

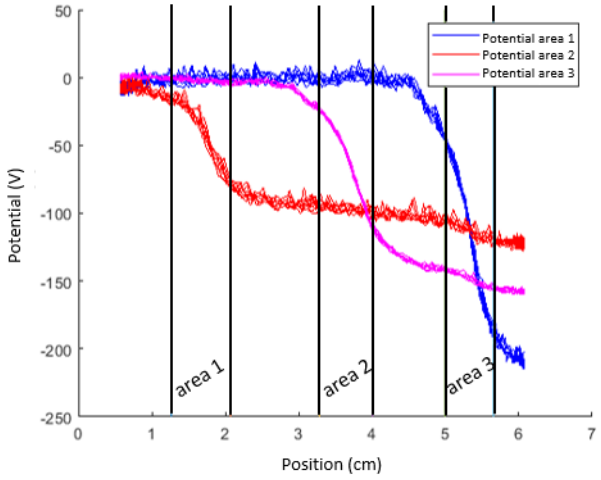

FIGURE 2 Comparison of surface potential between simulation under Comsol (a) and the experiment (b).

III. Perspectives

The next step of these experiments is the addition of resistive and capacitive loads in order to compare the performance of a TENG alone and one coupled with a DEG. Some preliminary tests represented on FIGURE 2 have been performed with a wide range of resistor values. Those curves remind the fact that TENG present a large internal impedance, and that to optimize the power transfer, a load of few hundreds of ohms is required as the area described by the QV cycle is the widest.

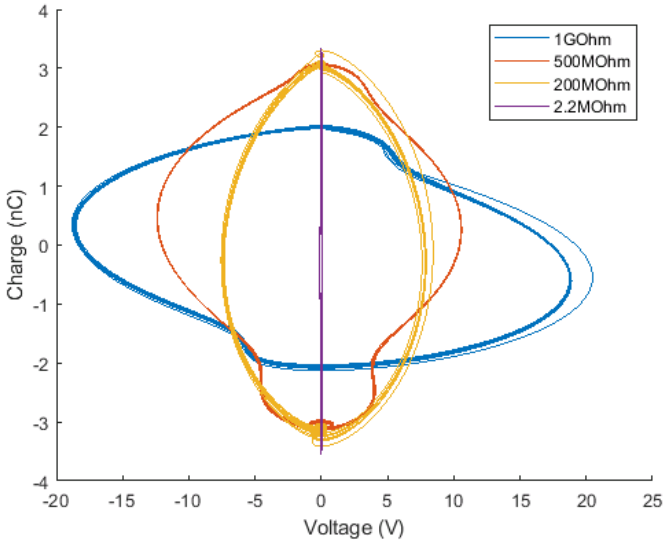

FIGURE 3. QV cycles for various loads

The other important aspect is the power conditioning, as the TENG is destined to charge a DEG, which is a variable capacitor. For that, different, different conditioner topologies already studied at Esycom laboratory [2] will be tested.

Acknowledgment

The first author would like to thank the GDR Nanomaterials for energy applications that allowed visiting Esycom laboratory and learning from the experiments performed there. S-E. Haim would also like to thank Pr Philippe Basset and Dr Armine Karami from this laboratory with whom he had very interesting discussions that enlightened on the advancement of this work.

References

[1] T Vu-Cong et al 2013. Electrets substituting external bias voltage in dielectric elastomer generators: application to human motion. Smart Mater. Struct. 22 025012

[2] C. Lagomarsini et al, 2019. Hybrid piezoelectric–electrostatic generators for wearable energy harvesting applications. Smart Materials and Structures, 28(3), p.035003.

[3] S. Wang et al,"Sliding-Triboelectric Nanogenerators Based on In-Plane Charge-Separation Mechanism", Nano Letters, vol 13,pp. 2226-2233, 2013.

[4] A. Ghaffarinejad et al," Superior performance of half-wave to full-wave rectifier as a power conditioning circuit for triboelectric nanogenerators: Application to contact-separation and sliding mode TENG", Nano Energy, 2019

Heat sink implementation on micro-thermoelectric generators (µTEGs) for power enhancement

Alex RODRÍGUEZ-IGLESIAS[1], Denise ESTRADA-WIESE[1,2], Jose-Manuel SOJO[3], Marta FERNÁNDEZ-REGÚLEZ[1], Iñigo MARTÍN-FERNÁNDEZ[1], Alex MORATA[3], Albert TARANCON[3], Llibertat ABAD[1], Joaquín SANTANDER[1], Marc SALLERAS[1], Luis FONSECA[1].

[1]*Instituto de Microelectrónica de Barcelona (IMB-CNM), CSIC, Cerdanyola del Vallès, 08193, Spain*

[2]*(Currently) Instituto Nacional de Astrofísica, Óptica y Electrónica (INAOE), Puebla, 72840, México*

[3]*Institut de Recerca de l'Energia de Catalunya (IREC), Sant Adrià de Besòs, 08930, Spain*

e-mail: alex.rodriguez@imb-cnm.csic.es

I. INTRODUCTION

Internet of Things (IoT) is raising as one of the keystones of our society. The ability to gather information from our environment, and the subsequent analysis of the obtained data, enhances the decision-making processes and is crucial for our prosperity. One of the main needs of the IoT is the self-sustainable supply of energy to the sensors. Among the available environmental sources, heat can be harvested by means of thermoelectric devices.

Earlier, the group developed all-Si based µTEGs with planar architecture based on Si (or SiGe) nanowires (NWs) acting as the thermoelectric material [1,2]. This approach benefits from Si and MEMS technologies for the downsizing and scalability, and from the fact that Si is abundant and environmentally sound. Unfortunately, the thermal resistance from the suspended platform to the ambient has limited the power generated by the µTEG.

This work reports on a procedure to reliably place a heat sink on top of the µTEGs, and on the improvement of its output characteristics. The integration of the heat sink on top of the fragile suspended platforms has only been possible by means of an adapter, together with the development of a custom pick and place system.

With the integrated heat sink the ΔT across the NWs is kept higher and the power generated by the µTEGs increases to meet the requirements of IoT applications at the microscale (a power density of 10-100 µW/cm^2).

II. µTEG DEVICE

The µTEG is based on the integration of NWs arrays between two structures at different temperatures. The Si bulk rim is in contact with a heat source while the suspended platforms, supported by Si_3N_4 low thermally conductive membranes, remain isolated. This configuration stands for the basic structure of the µTEG. To enhance the voltage or the current of the device, several of these basic µTEG structures are compactly connected either in series or in parallel, maximizing the generated power per square centimeter (Fig.1). The footprint of the total µTEG is 7x7 mm^2, with an active area of 5.5x5.5 mm^2, corresponding the remaining area to the pads. The power provided by the µTEGs is limited by the thermal resistance from the suspended platform to the ambient and by the thermal and the electrical conduction of the NWs, which, at this scale, highly limit any real application if no heat sink is implemented [2-4].

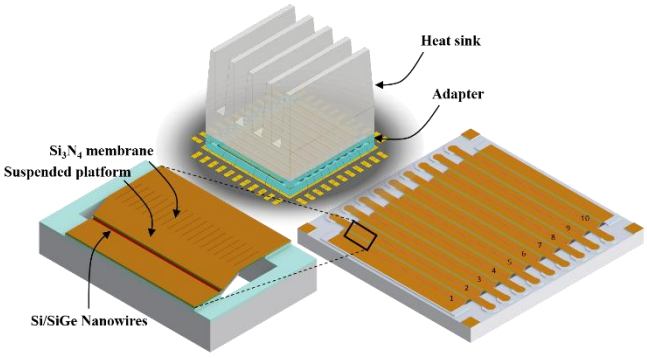

FIGURE 1. Si based µTEG. The right image corresponds to the total µTEG, composed by ten suspended platforms connected in series. An inset of the basic µTEG structure is represented on the left. It is composed by the suspended platform, supported by a Si_3N_4 membrane, and the trench, where the NWs array is grown. The upper image stands for the final device of this work, with the adapter and the heat sink implemented on top of the µTEG.

III. HEAT SINK IMPLEMENTATION

Unlike devices with a vertical thermoelectric structure [3,4], our planar µTEGs generate the ΔT on the device surface across the suspended membranes. A Si-based adapter has been designed and built, by means of microfabrication, as an interphase between the membranes and a heat exchanger to dissipate the heat from the membrane without cross thermal conduction from the bulk Si rim. A custom-pick & place has also been developed to place the adapter without breaking nor bending the membrane. The system is composed of two movable cameras and a microscope (located above the center of the setup) to provide the alignment in x, y and z directions, and a vacuum tweezer, with movement controls in x, y and z, to place softly an adapter, previously coated with a thermal paste, on top of the µTEG. The adapter, specifically designed for each type of µTEG, allows the use of the same commercial heat sink on every device and works as an intermediate step on the placement process. Due to its low weight and flat upper surface, it can be easily managed with the vacuum tweezer and placed without breaking the platforms. On its lower surface the adapter has several protuberances, those corresponding to the platforms and four pillars on the corners, to provide mechanical stability and a

wider distribution of the weight. After the drying of the thermal paste, the heat sink is deposited above the adapter with a live monitorization of the resistance of the device, in order to observe if any deformation is being done in the platforms. Thermal paste below the heat sink establishes the necessary thermal contact in between both surfaces.

IV. RESULTS

The performance of the µTEGs with and without heat sink (adapter + heat sink) are compared in Table 1 and Fig. 2 and 3. The increases in voltage and current are clearly visible when comparing the open circuit voltage (V_{oc}) and the short circuit current (I_{sc}) values of the generator during the three steps of the heat sink integration (Table 1, Fig. 2). Consequently, the maximum power, accomplished when device and load resistances match, is highly enhanced with the implementation of the heat sink.

The open circuit voltage of the µTEGs on a 250 ºC heat source, with and without heat sink, shows a multiplication factor of approximately 7, in still air convection, and 5, under a constant airflow of 1.3 m/s (equivalent to a natural breeze). The contribution of the heat sink regarding the air-heat sink heat exchange is the same for both cases, but a saturation point is reached under airflow conditions, as other thermal resistances (such as heat sink-adapter and adapter-platform) begin to limit the total heat exchange between the platforms and the air.

TABLE 1. Average V_{OC} and Max power data of the µTEGs with a 250 ºC heat source.

	V_{OC} (mV)	**Max power (µW/cm²)**
Bare µTEG (still air)	4,67 ± 0,21	0,37 ± 0,08
µTEG + Heat sink (still air)	31,66 ± 0,13	21,32 ± 3,61
Bare µTEG (1.3 m/s)	18,32 ± 2,37	6,32 ± 1,36
µTEG + Heat sink (1.3 m/s)	92,73 ± 11,58	194,57 ± 54,90

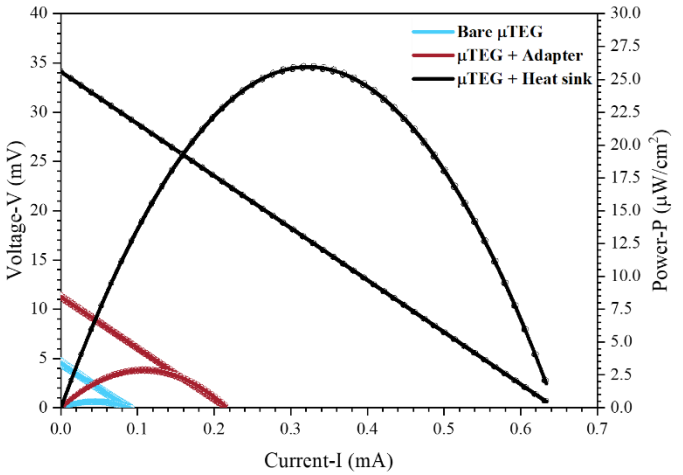

FIGURE 2. Voltage and Power generated by a Si NWs µTEG in the three steps of the Heat sink placement process, when in contact with a heat source at 250ºC and in still air convection.

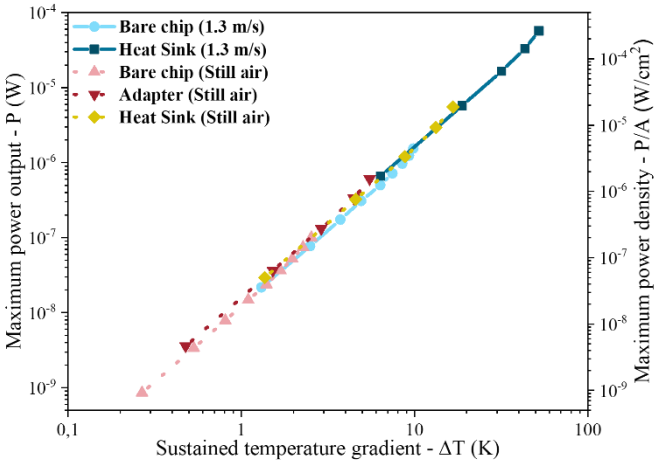

FIGURE 3. Power and power density of a Si NWs µTEG as a function of the ΔT across the NWs with both air convection conditions.

Fig. 3 presents the dependence of the output power as a function of the ΔT across the NWs in the three steps of the heat sink integration with both air convection conditions. In all the cases the Power vs ΔT curve remains the same, which demonstrates that the heat sink on top of the µTEGs only serves as an enhancer of the platforms heat exchange with the ambient. Its integration does not add parasitic heat flow paths nor increases the resistance values of the device. This second consequence implies that no damage nor bending is being done on the suspended platforms during the placement of the heat sink, as any of those would mean a change in the resistance value of the device.

V. CONCLUSIONS

The presented work demonstrates the utility of the heat sink as a heat exchange enhancer on the NWs based µTEGs. The power output of the µTEG with the heat sink matches the needs of IoT (10-100 µW/cm²) and becomes a feasible supplier for IoT applications at the microscale. Moreover, the obtained data proves that despite the challenging architecture of the device, the process set in place for the integration of the heat sink improves the performance, while not affecting the intrinsic characteristics of the designed µTEG. Thus, further investigation on the improvement of the heat sink itself and its thermal contact with the µTEG lays in front of us, in order to maximize the ΔT across the thermoelectric NWs and their generated power.

REFERENCES

[1] D. Estrada-Wiese et al., "Improved design of an all-Si based thermoelectric microgenerator," *Smart Systems Integration (SSI)*, pp. 1-4, 2021.

[2] M. Salleras et al., "Managing Heat Transfer Issues in Thermoelectric Microgenerators", in *Heat Transfer - Design, Experimentation and Applications. London, United Kingdom: IntechOpen*, 2021 [Online].

[3] Y. Shi et al., "Wearable Thermoelectric Generator With Copper Foam as the Heat Sink for Body Heat Harvesting," *in IEEE Access*, vol. 6, pp. 43602-43611, 2018.

[4] Settaluri, K.T. et al.. "Thin Thermoelectric Generator System for Body Energy Harvesting", *in J. Electron. Mater*, vol. 41, pp. 984–988, 2012.

High Rectification Ratio in Organic Diode Rectifier. Application in Flexible Energy Harvesting Rectenna.

Khaoula FERCHICHI *[1,2] , Baptiste GARNIER[1], Anthony Ozuem CHUCKWUKA[1], Sebastien PECQUEUR[1], David GUERIN [1], Ramzi BOURGUIGA[3], and Kamal LMIMOUNI*[1]

[1] *IEMN, CNRS, Université de Lille, Avenue Poincaré, BP 60069, 59652, Villeneuve d'Ascq, France.*

[2] *Univ. Littoral Côte d'Opale, EA 4476 - UDSMM - Unité de Dynamique et Structure de Matériaux Moléculaires, Dunkerque 59140, France.*

[3] *Laboratoire Physique des Matériaux, Structures et Propriétés Groupe Physique des Composants et Dispositifs Nanométriques, Faculté des sciences de Bizerte, Université de Carthage, Jarzouna-Bizerte 7021, Tunisia*

*corresponding author: Khaoula.ferchichi@univ-littoral.fr

***Abstract*—In this work, we demonstrate P3HT (poly 3-hexylthiophene) organic rectifier diode both in rigid and flexible substrate with a rectification ratio up to 10^6. This performance has been achieved through tuning the work function of gold with a self-assembled monolayer of 2,3,4,5,6- pentafluorobenzenethiol (PFBT). The diode fabricated on flexible paper substrate shows a very good electrical stability under bending tests and the frequency response is estimated at more than 20 MHz which is sufficient for radio frequency identification (RFID) applications. It is also shown that the low operating voltage of this diode can be a real advantage for use in a rectenna for energy harvesting systems. Simulations of the diode structure show that it can be used at GSM and Wi-Fi frequencies if the diode capacitance is reduced to a few pF and its series resistance to a few hundred ohms. Under these conditions, the DC voltages generated by the rectenna can reach a value up to 1 V.**

I. Introduction

Nowadays, diode rectifiers are a rapidly growing technology since it can be used in a range of applications such as radio frequency identification (RFID) tags, energy harvesting devices, and wireless communications. In particular, rectifiers from organic materials have attracted considerable attentions since they offer many advantages of low cost, flexibility, and soft processing.

Interface properties between electrodes and semiconducting materials play an important role to improve the performance of electronic devices. To achieve good hole injection within the organic semi-conductor layer, it is necessary to diminish the energetic difference between the electrode work-function and the organic semiconductor's highest-occupied molecular orbital (HOMO).

In this work, we investigate the effect of interface engineering with PFBT SAM in P3HT polymer diode rectifier on rigid and paper substrate. We use this strategy to increase the imbalance between the forward and reverse current of the diode and thus to improve the rectification ratio. The diode is fabricated on a release paper and can be transferred on any other flexible substrate.

II. Experimental

N type Si wafer (doped with phosphor, 380–400 μm thick, resistivity of 0.0001– 0.0003 Ω·cm) with 200 nm thermal oxide layer was used as substrate. The substrate was ultrasonically cleaned with acetone and isopropanol for 10 min each, and then treated by ultra-violet ozone for 25 min to remove any residual contaminants on the surface. With a 5 nm titanium adhesion layer, 120 nm Au were deposited by thermal evaporation through shadow mask to serve as anode contact. For SAM functionalization on the anode, samples were immersed in the solution of 10 μL of PFBT (Sigma-Aldrich, Saint Louis, MO, USA, purity 97%, molecular weight Mn = 15–45 kDA, polydispersity PDI ≤ 2) diluted in 10 mL of ethanol for 18 h, and followed by rinsing with pure ethanol and drying under nitrogen flow. After functionalization, the semiconductor was wet-deposited. The solution was prepared by dissolving 30 mg/mL of regioregular P3HT (Sigma-Aldrich 99.995%) in chlorobenzene, and coated in a glove box under a N_2 atmosphere at 1000 rpm for 30 s. The thickness was measured by profilometry to be 110 nm. The film was then backed for 1 h at 100 °C in vacuum to remove the remaining solvent. After the deposition of the semiconductor layer, 120 nm of Al was thermally evaporated through shadow mask to form top contacts. The overlap between Au and Al contacts defines the diodes' active area, ranging from 10^{-4} to 10^{-2} cm^2. One sample of P3HT diode without PFBT treatment was fabricated as a reference.

III. Results and Discussion

Current density voltage (J-V) characteristics of P3HTdiode rectifiers with and without PFBT are shown in Figure 1a. The current density is about 0.1 A/cm^2 at 4 V for the diode the diode with PFBT one order of magnitude higher than the diode without PFBT. We can also evaluate from this figure the rectification ratio R defined as the ratio between ON and OFF currents at a fixed voltage. R was measured for 13 devices as presented in the histogram of Figure 1b. The rectification ratio reaches 10^6 at ±4V for P3HT diodes with PFBT and spreads from 10^2 to 10^6

without SAM functionalization. Few diodes without SAM shows slightly higher rectification, but only due to the particularity low noise current.

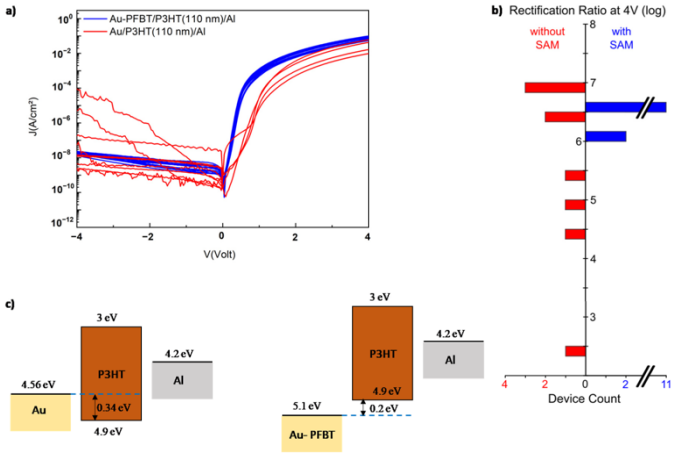

Figure 1. (a) J-V characteristics of diodes with and without PFBT functionalization, (b) rectification ratio collected from 13 diodes, (c) energy band diagram of the device.

This performance improvement can be attributed to two different properties for the PFBT treatment: a first one is the energy barrier reduction between gold and HOMO level of organic semiconductor and the second one is a change in the semiconductor film morphology and molecular orientation.

On another level and to demonstrate the possible flexibility of our devices, the Au- PFBT/P3HT/Al diode has been fabricated on flexible substrate, which is a cardboard paper provided by Centexbel (ref WO84). This paper has the advantage to possess a small roughness of about 1.4 nm due to a protective coating of silicone, and showed high stability to the solvent that are employed in the diode fabrication process. The paper was first placed in a primary vacuum oven at 100 ◦C for 1 h to degas the moisture present in the fibers. The diode was then fabricated on this substrate with the same process for silicon oxide substrate. In addition, this paper substrate is a release paper that can allow an easy transfer to all other flexible substrates such as textiles.

The electrical characteristic of the diode fabricated on the release paper is shown by Figure 2. A density current of 0.026 A/cm^2 was obtained at 4 V and high rectification ratio of 4×10^5 at ±4 V. The flexible diode rectifier is measured under bending tests with radius of 1.4 cm. The results show very good stability of the electrical characteristic except a little increase of the OFF current. This can be related to the direction of the bending that was made parallel to the aluminum electrode.

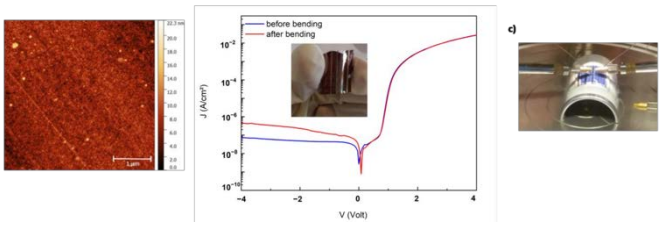

Figure 2. (a) AFM of the paper substrate, (b) J-V characteristic of the diode before and after bending, (c) photograph of measurement approach under bending (curvature radius 1.4 cm).

The frequency response of the diode rectifier was also evaluated by LT-Spice simulation tools using the basic circuit rectifier. The parameters of the diode used in simulation are extracted experimentally by impedance spectroscopy measurements. Under a 500 kHz, 2 V peak-to-peak oscillating input signal, an output DC voltage of 1.51 V was obtained, value that decreases to reach a DC output voltage of 0.15 when the input frequency increases to 20 MHz which is compatible with RFID applications (13.56 MHz). For energy harvesting, the frequency response of the diode is improved by optimizing the device structure with reducing the capacitance of the diode and its resistance.

IV. Conclusion

In this study, high rectification ratio up to 10^6 has been achieved for P3HT diode rectifier on silicon substrates and through the tuning of the work function of gold electrode anode by a self-assembled monolayer of PFBT. The P3HT rectifier diodes were also fabricated on flexible substrate (Centexbel release paper). They on paper demonstrated also a good rectification ratio and electrical stability under bending tests. By reducing the resistance and capacity of the organic diode structure, we demonstrate that these diodes can be used in a rectenna for energy harvesting systems.

Acknowledgment

This work was financially supported by the European Project Interreg Luminoptex and the French ANR Context project (grant number ANR-17-CE24-0013).

References

[1] K. Ferchichi et al., High Rectification Ratio in Polymer Diode Rectifier through Interface Engineering with Self-Assembled Monolayer. *Electron. Mater. 2021*, 2, 445–453. https://doi.org/10.3390/electronicmat2040030

Investigations sur la modélisation d'un récupérateur à empilement piézoélectrique amplifié

Anthony CASISA[1*], Barbara LAFARGE[1], Vincent LANFRANCHI[1], Christophe DELEBARRE[2], Sébastien GRONDEL[2]

[1] *Université de technologie de Compiègne, laboratoire Roberval (Mechanics, energy and electricity), centre de recherche de Royallieu – CS 60319 – 60203 Compiègne Cedex - France*

[2] *Univ. Polytechnique Hauts-de-France, CNRS, Univ. Lille, UMR 8520 - IEMN - Institut D'Electronique de Microélectronique et de Nanotechnologie, F-59313, Valenciennes, France*

*corresponding author e-mail : anthony.casisa@utc.fr

***Abstract*—Les récupérateurs d'énergie de type « empilement piézoélectrique amplifiés » ont comme principale caractéristique de multiplier la tension générée à basse fréquence. La conception de la structure amplificatrice est déterminante pour le choix des fréquences de résonance du récupérateur. Afin de caractériser ce type de structure, nous calculons numériquement ces fréquences. Une validation expérimentale est ensuite proposée. Les résultats de cette investigation démontrent que l'empilement piézoélectrique peut récupérer jusqu'à 3.1mW sous une excitation de 8m/s² à la fréquence de 324 Hz.**

I. INTRODUCTION

Pour récupérer l'énergie mécanique ambiante, les matériaux piézoélectriques offrent une meilleure densité de puissance que les autres solutions courantes. En particulier, les empilements piézoélectriques amplifiés améliorent les performances des empilements seuls. Ils facilitent par exemple la récupération d'énergie mécanique issue de la marche humaine [1], [2].

La modélisation analytique de l'empilement piézoélectrique est abondamment documentée dans la littérature, notamment par le modèle équivalent masse-ressort à un degré de liberté (SDOF) [1]–[3]. La modélisation analytique de la structure amplificatrice est généralement vérifiée dans le cas quasi-statique, ou avec des excitations non harmoniques [1]–[4].

Cette étude porte sur un récupérateur d'empilement piézoélectrique amplifié. Elle présente le modèle analytique multiphysique de l'empilement, le modèle numérique de l'amplificateur, et la validation expérimentale des fréquences de résonance simulées.

II. MODELISATION DU RECUPERATEUR

A. *Description globale du récupérateur*

Le récupérateur APA600M de Cedrat Technologies [5] étudié ici est présenté en Figure 1. Il est composé d'un empilement piézoélectrique et d'une structure métallique (l'amplificateur).

B. *Modélisation analytique de l'empilement*

Les équations constitutives piézoélectriques sont en Eq. (1). :

$$\begin{cases} S_{33}(t) = s_{33}^{E} T_{33}(t) + d_{33} E_3(t) \\ D_3(t) = d_{33} T_{33}(t) + \varepsilon_{33}^{T} E_3(t) \end{cases} \quad (1)$$

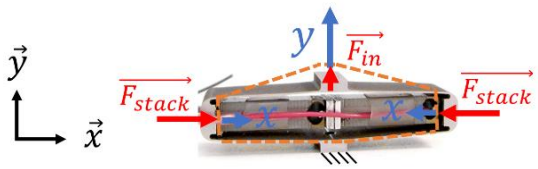

Figure 1 : APA 600M – notations et conditions aux limites

Avec S la déformation de l'empilement, T la contrainte sur l'empilement, E le champ électrique, et D l'induction électrique de l'empilement. Les constantes sont la souplesse s_{33}^{E}, la constante piézoélectrique d_{33}, et la permittivité ε_{33}^{T} [6]. Le principe fondamental de la dynamique sur la structure et l'application d'une charge résistive aux bornes de l'empilement conduisent à l'Eq. (2) :

$$\begin{cases} m_{eff}\ddot{x} + kx - \dfrac{d_{33} kn}{C_0} Q = F_{stack}(t) \\ R\dot{Q} - \dfrac{d_{33} kn}{C_0} x + \dfrac{Q}{C_0} = 0 \end{cases} \quad (2)$$

Avec m_{eff} la masse équivalente de l'empilement, k la raideur de l'empilement en compression, n le nombre de couches piézoélectriques, C_0 la capacité à vide de l'empilement, et R la résistance de charge. x est le déplacement de l'empilement (Figure 1), Q est la charge électrique de l'empilement ($i = \dot{Q}$), et F_{stack} est la force appliquée sur l'empilement [1].

Soit F_{stack} une force sinusoïdale de fréquence f. La puissance générée est maximale à la résistance optimale définie par l'Eq. (3) :

$$R_{opt} = \frac{1}{2\pi C_0 f} \quad (3)$$

La force d'excitation du récupérateur est F_{in}. Le rapport entre la force résultante F_{stack} et la force d'excitation F_{in} est constant dans le domaine quasi-statique ($F_{stack} = M * F_{in}$ [1], [2]). Ce rapport varie à des fréquences plus élevées [4]. Nous avons fait le choix d'une étude numérique par éléments finis de l'amplificateur pour étudier ses trois premières fréquences de résonance.

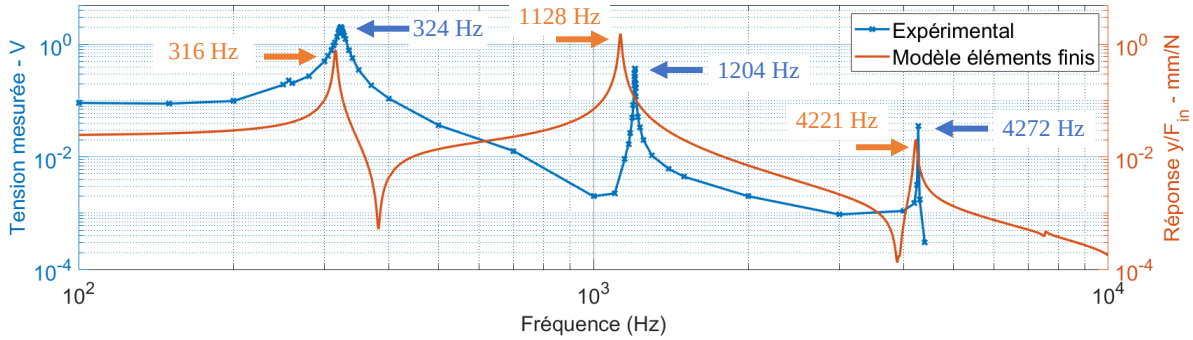

Figure 2 : réponses en fréquence du APA600M expérimentale et numérique

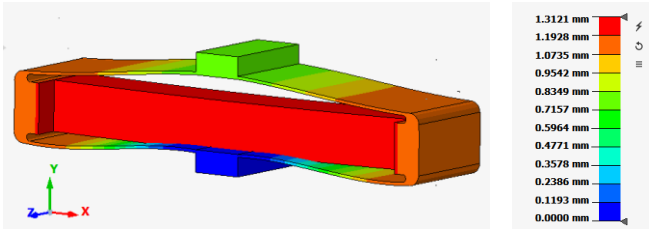

Figure 3 : déformée du APA à 316 Hz (1er mode)

C. Modélisation mécanique éléments finis de l'amplificateur

Le récupérateur est modélisé sous le logiciel éléments finis Altair Simlab. La masse volumique de l'ensemble est de 7850kg/m^3 ; le module d'Young de l'empilement et de l'amplificateur sont respectivement de 44GPa et 208GPa. Les conditions aux limites sont un encastrement et une force d'excitation F_{in} (Figure 1). L'amplitude de F_{in} est égale à 1N. La fréquence varie sur l'intervalle [1-16 000 Hz].

Les trois premiers modes dans la direction $\vec{y}$ sont calculés à 316Hz (Figure 3), 1128Hz et 4221Hz. Nous allons retrouver ces fréquences de résonance expérimentalement.

III. Experimentations sur pot vibrant

Le récupérateur APA600M est excité par un pot vibrant. La face inférieure suit une accélération d'amplitude environ 8m/s², de fréquence variable sur [100-5000 Hz]. La face supérieure est laissée libre. On fait l'hypothèse que ces conditions aux limites donnent un comportement similaire à celles de la Figure 1.

Dans un premier temps, la tension générée par le récupérateur est observée en circuit ouvert. La réponse en fréquence expérimentale (tension) du récupérateur est comparée à la réponse en fréquence simulée (déplacement) en Figure 2. Les trois premières fréquences de résonance expérimentales sont proches des fréquences simulées : 324 Hz (+3%), 1204 Hz (+7%), et 4272 Hz (+1.2%).

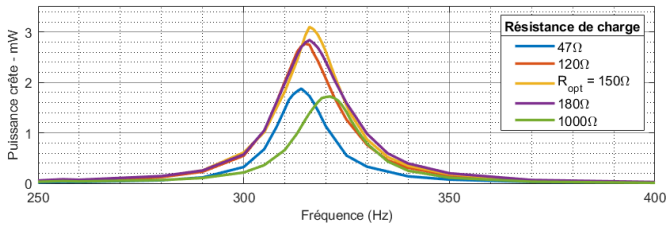

Figure 4 : spectre de puissance générée sur charge résistive

Dans un second temps, la tension générée sur la charge résistive est observée (Figure 4). La résistance obtenue par l'Eq. (3) est environ R_{opt} = 150Ω pour C_0 = 3.2µF et f = 324Hz. C'est à cette valeur que la puissance est maximale. On obtient 3.1mW à la résonance.

IV. Conclusion

Le modèle mécanique en éléments finis prédit le comportement résonant de l'empilement piézoélectrique amplifié pour les trois premiers modes. Dès lors, il est possible de concevoir une structure d'empilement piézoélectrique amplifiée dont la fréquence de résonance s'accorde avec l'excitation mécanique vibratoire ambiante. Cette optimisation conviendrait aux moteurs industriels, typiquement alimentés à 50Hz, qui génèrent des vibrations à 100Hz.

En termes de performance, le récupérateur emmagasine jusqu'à 3.1mW pour une résistance électrique optimale de 150Ω, et une excitation de 8m/s² autour de 320Hz.

En perspective, il serait souhaitable de trouver une modélisation analytique (à un ou plusieurs degrés de liberté) qui satisfasse la précision du modèle numérique avec plus de rapidité.

References

[1] J. Feenstra, J. Granstrom, et H. Sodano, « Energy harvesting through a backpack employing a mechanically amplified piezoelectric stack », *Mechanical Systems and Signal Processing*, vol. 22, nº 3, p. 721-734, avr. 2008, doi: 10.1016/j.ymssp.2007.09.015.

[2] F. Qian, T.-B. Xu, et L. Zuo, « Design, optimization, modeling and testing of a piezoelectric footwear energy harvester », *Energy Conversion and Management*, vol. 171, p. 1352-1364, sept. 2018, doi: 10.1016/j.enconman.2018.06.069.

[3] A. J. Lee, Y. Wang, et D. J. Inman, « Energy Harvesting of Piezoelectric Stack Actuator From a Shock Event », *Journal of Vibration and Acoustics*, vol. 136, nº 1, p. 011016, févr. 2014, doi: 10.1115/1.4025878.

[4] D.-X. Cao, X.-J. Duan, X.-Y. Guo, et S.-K. Lai, « Design and performance enhancement of a force-amplified piezoelectric stack energy harvester under pressure fluctuations in hydraulic pipeline systems », *Sensors and Actuators A: Physical*, vol. 309, p. 112031, juill. 2020, doi: 10.1016/j.sna.2020.112031.

[5] « Amplified piezo actuator - APA600M - CEDRAT TECHNOLOGIES ». https://www.cedrat-technologies.com/en/products/product/APA600M.html (consulté le 20 mai 2022).

[6] M. Brissaud, *Matériaux piézoélectriques: Carctérisation, modélisation et vibration*, Première édition. Presses polytechniques et universitaires romandes, 2007.

Numerical simulations of acoustic power transfer

Pierre TACYNIAK[1,*], Martial DEFOORT[1] and Skandar BASROUR[1]

[1] *Univ. Grenoble Alpes, CNRS, Grenoble INP, TIMA, 38000 Grenoble, France*

* pierre.tacyniak@univ-grenoble-alpes.fr

Abstract—Wireless power transfer is currently studied in the biomedical field to miniaturize medical implants. In this paper, two models of the power transfer through an intermediate layer were designed and compared on Python and Pspice. A study was carried out about the different physical effects involved in the transmission and a preliminary experiment confirmed the relevance of our models.

I. Introduction

Wireless Power Transfer (WPT) is a solution commonly used to recharge everyday objects such as smartphones. The technology used for these purposes is usually induction.

However, WPT is studied in other fields such as biomedical engineering in order to recharge medical implants. For this particular case, A. Denisov *et al* [1] showed that Acoustic Power Transfer (APT) is more efficient than induction for deeply implanted and miniaturized medical implant. Moreover, as the body is composed of 65% water, the electromagnetic losses increase due to eddy currents [2]. As medical implants and battery sizes shrink, WPT and piezoelectric technologies are currently the subject of many studies [3] and are a promising solution.

This manuscript describes first a study of the APT model using Python and Pspice software followed by an analysis of the numerical results obtained. In a last part a preliminary experimental result was carried out.

II. Modelling the wireless power transfer

Based on Mason model, the acoustic behavior of a layer of material can be modelled as a quadrupole. A piezoelectric transducer, on the other hand, can be modelled as an hexapole composed of two parts: a mechanical part, corresponding to the former acoustic quadrupole and an electrical part, related to the piezoelectric conversion.

A. Python model

Hence, the power transfer channel can be modeled by a single matrix composed of the different Mason's matrix of each layer:

$$\begin{pmatrix} F_1 \\ F_2 \\ u_1 \\ -F_2 \\ F_3 \\ -F_3 \\ F_4 \\ u_2 \end{pmatrix} = \begin{pmatrix} X_{11}^1 & X_{12}^1 & X_{13}^1 & 0 & 0 & 0 & 0 & 0 \\ X_{12}^1 & X_{11}^1 & X_{13}^1 & 0 & 0 & 0 & 0 & 0 \\ X_{13}^1 & X_{13}^1 & X_{33}^1 & 0 & 0 & 0 & 0 & 0 \\ 0 & 0 & 0 & X_{11}^2 & X_{12}^2 & 0 & 0 & 0 \\ 0 & 0 & 0 & X_{12}^2 & X_{11}^2 & 0 & 0 & 0 \\ 0 & 0 & 0 & 0 & 0 & X_{11}^3 & X_{11}^3 & X_{11}^3 \\ 0 & 0 & 0 & 0 & 0 & X_{11}^3 & X_{11}^3 & X_{11}^3 \\ 0 & 0 & 0 & 0 & 0 & X_{11}^3 & X_{11}^3 & X_{11}^3 \end{pmatrix} \begin{pmatrix} V_1 \\ V_2 \\ i_1 \\ V_3 \\ V_4 \\ V_5 \\ V_6 \\ i_2 \end{pmatrix} \quad (1)$$

Where F, u, V, i, X^m are respectively, the force, the voltage, the speed of propagation, the current and the impedance of the layer m, as seen in FIGURE 1. O. Freychet *et al* [4], demonstrated that it is possible to deduce the gain between u_2 and u_1:

$$\frac{u_2}{u_1} = \frac{Z_{Load}}{Z_A(Z_{Load} + Z_B)/Z_C - Z_C} \quad (2)$$

Where Z_A, Z_B, Z_C are equivalent impedances developed in [4]. Implementing this model on Python allows to obtain a closed-form model usable for any custom stack.

B. Pspice model

In order to design more concretely systems and optimize their power transmission, a second simulation was done by simulating directly the Mason model (FIGURE 1 (B)) with Pspice based on T-line with losses model [5]. This model has the advantage to quickly fit systems to desired functions and to give the components needed to create the system in real life.

C. Pspsice/Python comparison

Aiming to see if both models give the same results, a comparison was carried out on a three-layer system composed of two PZT PIC181 transducers with a diameter of 45 mm and a 6 mm thick aluminum plate with a $Z_{load} = 20\Omega$.

We observe a quantitative agreement between the two models with a maximum resonance frequencies mismatch of 0.6%. However, the Python simulation seems to underestimate the losses which will need further investigations.

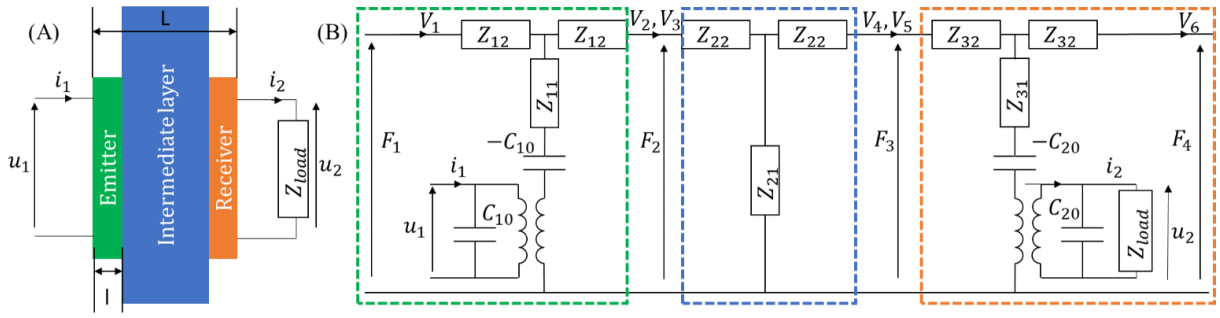

FIGURE 1. (A) SCHEMATIC OF A 3-LAYER ACOUSTIC POWER TRANSFER SYSTEM AND (B) ITS MASON EQUIVALENT MODEL.

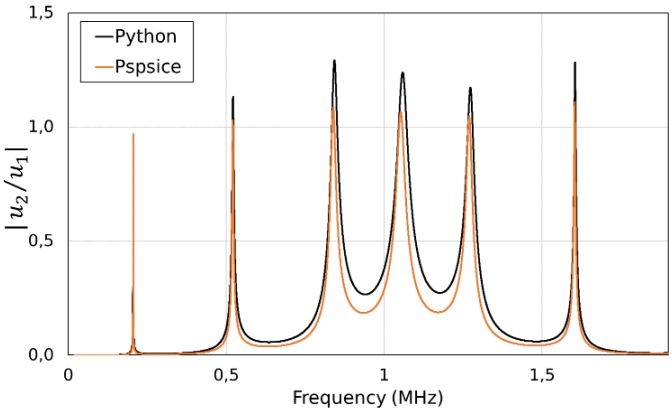

FIGURE 2. COMPARISON BETWEEN PYTHON AND PSPICE SIMULATIONS FOR A 3-LAYER MODEL

D. Analysis of the results provided by the simulations

So as to dimension future systems, it is necessary to understand what are the different physical effects shaping the curves obtained. For this purpose, an analysis was done with Python by considering three layers of PZT where the piezoelectric properties of the intermediate layer were cancelled (FIGURE 3).

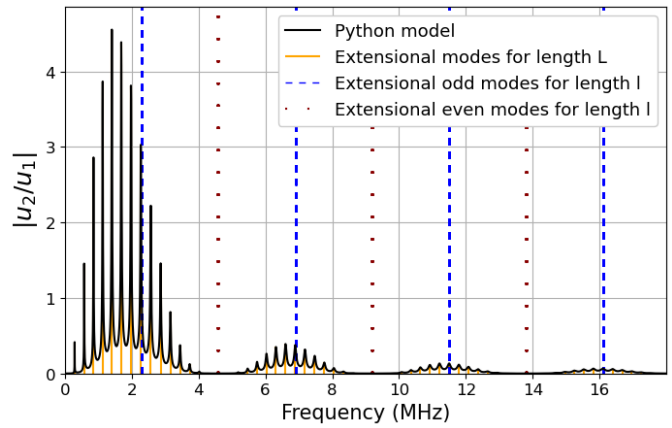

FIGURE 3. PYTHON SIMULATION FOR A 3-LAYER PZT SYSTEM WITH NO-PIEZOELECTRIC PROPERTIES ON THE INTERMEDIATE LAYER.

Looking back at FIGURE 1, we observe three phenomena:

- The orange peaks are evenly spaced by a frequency equal to the resonance frequency of the first extensional mode of the whole system of length L.
- The "modulation" is aligned around the odd extensional modes of the piezoelectric layers of length l (blue lines).
- The attenuation at the even modes of the piezoelectric layers are due to the fact that these modes are symmetric and thus not visible (red dots).

III. PRELIMINARY EXPERIMENTAL RESULT

A. Experimental setup

A first measure was carried out with a 3-layer system composed of two 0.2 mm-thick piezo ceramic Noliac NCE51 with a diameter of 12.8 mm and an intermediate layer of tungsten 3.2 mm thick with a square shape of 50 × 50 mm. A load of 20 Ω was put in parallel of the piezoelectric receiver. The measurement was done on an Agilent Technologies E5061B network analyzer.

B. Results

We observe in the experimental results of FIGURE 4 similar results than those obtained with the numerical simulation of FIGURE 2 as most of the peaks are equally spaced.

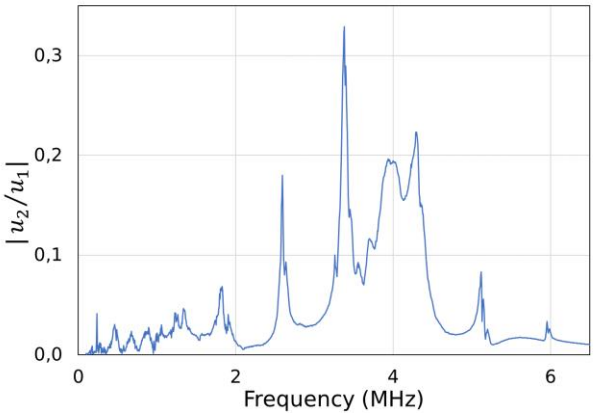

FIGURE 4. FREQUENCY RESPONSE OF A 3-LAYER SYSTEM MADE WITH AN INTERMEDIATE LAYER OF TUNGSTEN AND NOLIAC NCE51 TRANSDUCERS

However, we observe modes at low frequencies which are probably non-extensional modes of the intermediate layer and are not taken into account in the simulations.

IV. CONCLUSION

Starting from a Python model, we were able to gain insight on the frequency response of an APT system regarding its dimensions. We could then compare it with a more design-oriented Pspice model. We performed a preliminary experiment that confirms the relevance of our models and will allow us to simulate more complicated models such as human tissue. In order to obtain a more realistic and comprehensive model including all resonance modes, a Finite Element analysis will also be designed in the near future.

REFERENCES

[1]. A. Denisov & E. Yeatman, "Ultrasonic vs. Inductive Power Delivery for Miniature Biomedical Implants," *2010 International Conference on Body Sensor Networks*, pp. 84-89, 2010.

[2]. P. Liu, T. Gao, & Z. Mao, "Analysis of the Mutual Impedance of Coils Immersed in Water", *Magnetochemistry 2021*, 7, 2021.

[3]. H. Basaeri, D. B. Christensen, & S. Roundy, "A review of acoustic power transfer for bio-medical implants". *Smart Materials and Structures*, *25*(12), 2016.

[4]. O. Freychet, F. Frassati, S. Boisseau, N. Garraud, P. Gasnier, & G. Despesse, "Analytical optimization of piezoelectric acoustic power transfer systems", *Engineering Research Express*, *2*(4), 2020.

[5]. R. S. Dahiya, M. Valle & L. Lorenzelli, "SPICE model for lossy piezoelectric polymers," *IEEE Transactions on Ultrasonics, Ferroelectrics, and Frequency Control*, vol. 56, no. 2, pp. 387-395, 2009.

Stress cycle on a ZnO nanowire-based nanogenerator: a phenomenological study

Emmanuel DUMONS[1*], Guylaine POULIN-VITTRANT[1] and Louis Pascal TRAN-HUU-HUE[1]
[1] *GREMAN UMR 7347, CNRS, Université de Tours, INSA CVL, 3 rue de la Chocolaterie 41000 BLOIS*
*emmanuel.dumons@insa-cvl.fr

***Abstract*—Energy harvesting using nanogenerators is a complex process that starts with the scavenged mechanical energy and ends with the electrical energy given to a load. During this process, many phenomena appear at different steps and in different parts of the device. This work shows with an original point of view that in nanogenerators, energy conversion depends on intrinsic parameters such as zinc oxide doping level or polymer dielectric permittivity. By considering the whole energy conversion chain, this study investigates the important characteristic times adaptation between mechanical excitation and electrical transfer to load.**

I. Introduction

Mechanical energy harvesters are promising devices to make integrated sensors or actuators autonomous by scavenging free energy from the environment [1]. Piezo-nanogenerators use direct piezoelectric effect to harvest an external mechanical energy and convert it into electrical one. For this purpose, ZnO (zinc oxide) nanostructures are used as piezoelectric material and are embedded within a polymer matrix. Many additional phenomena appear during the energy conversion within these nanogenerators: the ZnO semiconducting properties create screening effect due to the free charge carriers and surface effects, the polymer has mechanical and electrical influence [2]…

The aim of this work is to search influent parameters on the energy conversion and transfer to the external load such as mechanical excitation time-dependence, ZnO doping level, polymer dielectric permittivity and external load resistance.

II. Device and model description

A. Nanogenerator

To harvest external mechanical energy, the nanogenerators considered here have ZnO piezo-semiconductive vertical nanowires as active elements embedded in a polymer matrix. Including the substrate and the electrodes, these nanogenerators are five-layer devices that electrically work in a capacitive mode due to the polymer layer on the top of the nanowires [3].

B. Unit cell for simulations

To study the different physical phenomena involved in the energy harvesting process, the nanogenerator is studied through a 2D-axisymmetric unit cell composed of a single ZnO nanowire with a polymer layer above. This single cell study allows to predict the full device performance [4]. Due to the unit cell geometry and to the kind of mechanical excitation, we can consider that the piezoelectric material is excited in the 33-mode only. Metallic top and bottom electrodes allow connecting this unit cell to an external circuit. The role of the substrate is not studied in this model. Simulations are performed with *COMSOL Multiphysics*® using our custom-made simulation module coupling piezoelectric and semiconducting properties of ZnO. The geometric parameters are kept constant in the present study as they were studied previously [5].

C. Stress cycle and boundary conditions

The external mechanical excitation onto this unit cell is a four-step variable pressure applied on top of the unit cell (increasing ramp, constant pressure, decreasing ramp and zero pressure, all of them having the same duration τ_m). It creates a stress cycle on the unit cell. The boundary conditions are reported in TABLE 1.

TABLE 1. Unit cell boundary conditions

	Boundary conditions	
Unit cell boundaries	***Mechanical***	***Electrical***
Polymer top surface	Pressure	Circuit terminal (top electrode)
Polymer lateral surface	Free	Zero charge
Polymer/ZnO interface	Continuity	Insulator interface
ZnO lateral surface	Free	Insulation
ZnO bottom surface	Roller	Ohmic contact (bottom electrode)

D. Connection to an external circuit

In the present study, the harvested energy is transferred from the nanogenerator to a resistor *R* representing the electrical load. The harvested energy is then only dissipated by Joule effect during the discharge of the unit cell. This phenomenon introduces a new time τ_e that corresponds to an electrical characteristic time.

III. Results and discussion

A. Electrical energies evolution

Because of the direct piezoelectric effect, a polarization appears within the nanowire and creates an electric field in the unit cell.

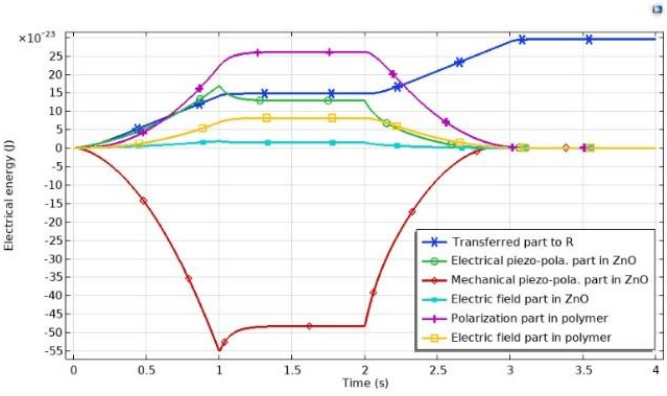

FIGURE 1. Electrical energies evolution

FIGURE 1 presents the evolution of the different electrical energies in the nanowire and in the polymer due to the pressure variation. The graph also includes the amount of energy transferred to the external circuit (dark blue curve).

B. *Electrical cycle (E_3,D_3)*

To better assess the efficiency of energy transfer to external load, the electrical cycle (E_3,D_3) area in J.m^{-3} represents:

$$\omega_{el} = \oint D_3 dE_3 \quad (1)$$

the electrical energy density stored in the ZnO nanowire. The local fields are evaluated at the center of the nanowire in order to plot the cycle in FIGURE 1. The electrical cycle presents also four steps corresponding to the mechanical cycle ones.

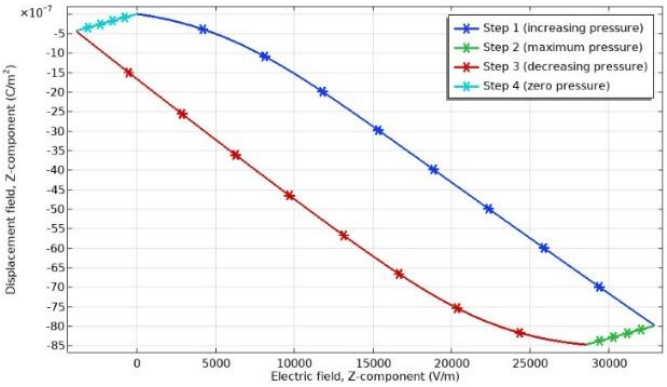

FIGURE 2. ELECTRICAL CYCLE

C. *Influence of the ZnO doping level*

Due to the semiconductive properties of ZnO, the screening effect of the piezopotential occurs and decreases the harvested energy. The ZnO doping level depends on the nanowires fabrication process [6]. The area of the electrical cycle decreases when the doping level increases.

D. *Influence of the polymer dielectric permittivity*

The polymer dielectric permittivity is an important parameter due to the capacitive effect introduced by the polymer layer above the ZnO nanowires. The higher the polymer dielectric permittivity, the higher electrical energy transferred to the load as shown in FIGURE 1.

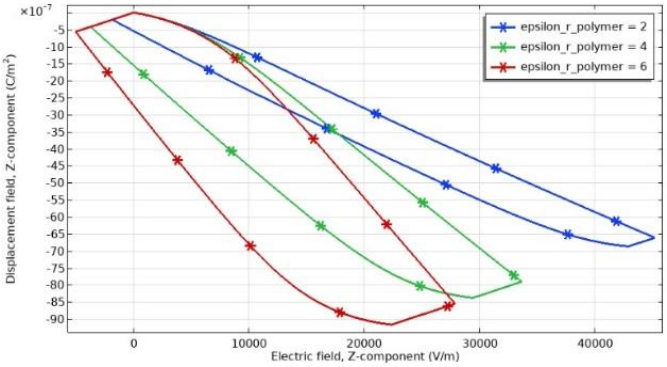

FIGURE 3. ELECTRICAL CYCLE FOR DIFFERENT POLYMER DIELECTRIC PERMITTIVITIES

E. *Influence of the external load*

By modifying the resistance of the external load, we modify the electrical characteristic time τ_e of the phenomenon. Therefore, we can study the influence of this parameter on the electrical cycle and on the amount of harvested energy. Simulations show that there is a match between the two characteristic times τ_e and τ_m to maximize the efficiency of the electrical transfer to the external load (FIGURE 1). This result reinforces the interest of using controllable electrical circuits with switching techniques in order to adapt τ_e to τ_m imposed by the external mechanical excitation [7].

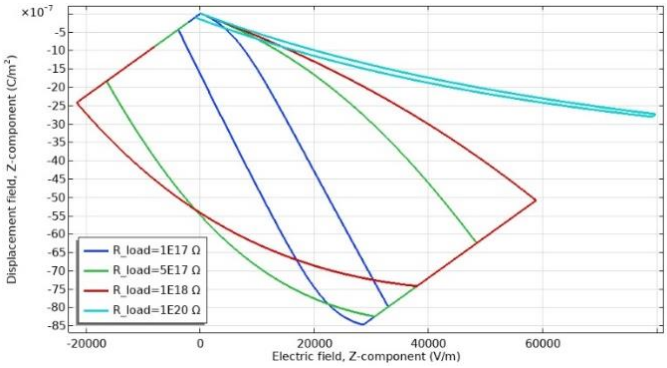

FIGURE 4. ELECTRICAL CYCLE FOR DIFFERENT LOAD RESISTANCES

The cycle with maximum area (red one) indicates the optimal resistance value for a unit cell. By dividing this one by the nanowires number (around one billion) of the prototype described in [3], the full nanogenerator optimal resistance can be estimated [4].

IV. CONCLUSION

Thanks to our simulation tool including coupled physics, this original study of the piezo-semiconducting nanostructure explains the different phenomena involved within the nanogenerator. This provides a better understanding of the full energy harvesting process, combining mechanical energy conversion and electrical charges extraction. This transient analysis opens perspectives to take into account even more realistic mechanical cycles in specific applications. It also shows the influencing parameters that have a real impact on the amount of converted and transferred energy to an external resistor. This time-dependent study will be completed by considering losses in the different materials and ZnO surface traps [5]. Furthermore, other external loads will be used to get closer to a typical circuit following the nanogenerator.

REFERENCES

[1] S. Sripadmanabhan Indira, C. Aravind Vaithilingam, K. S. P. Oruganti, F. Mohd, & S. Rahman, « Nanogenerators as a Sustainable Power Source: State of Art, Applications, and Challenges », *Nanomaterials*, vol. 9, n° 5, p. 773, May 2019.

[2] A. T. Le, M. Ahmadipour, & S.-Y. Pung, « A review on ZnO-based piezoelectric nanogenerators: Synthesis, characterization techniques, performance enhancement and applications », *Journal of Alloys and Compounds*, vol. 844, p. 156172, Dec. 2020.

[3] T. Slimani Tlemcani, C. Justeau, K. Nadaud, D. Alquier, & G. Poulin-Vittrant, « Fabrication of Piezoelectric ZnO Nanowires Energy Harvester on Flexible Substrate Coated with Various Seed Layer Structures », *Nanomaterials*, vol. 11, n° 6, Art. n° 6, Jun 2021.

[4] N. Doumit & G. Poulin-Vittrant, « A New Simulation Approach for Performance Prediction of Vertically Integrated Nanogenerators », *Advanced Theory and Simulations*, vol. 1, n° 6, p. 1800033, 2018.

[5] E. Dumons, G. Poulin-Vittrant, & L. P. Tran-Huu-Hue, « Theoretical study of electro-mechanical energy conversion in ZnO nanowire-based nanogenerator », *Presented at the JNRSE 2021 10th National Days on Energy Harvesting and Storage 2021*, p. 33, 2021.

[6] A. J. Lopez Garcia, M. Mouis, V. Consonni, & G. Ardila, « Dimensional Roadmap for Maximizing the Piezoelectrical Response of ZnO Nanowire-Based Transducers: Impact of Growth Method », *Nanomaterials*, vol. 11, n° 4, Art. n° 4, Apr. 2021.

[7] G. Poulin, F. Costa, E. Sarraute, & E. Minazara, « Non linear method for the amplification of electrical power delivered by a piezoelectric generator », *Eur. Phys. J. Appl. Phys.*, vol. 33, n° 2, p. 121-132, Feb 2006.

Transducer Interfacing Circuits for Electrostatic Near-Limits Kinetic Energy Harvesting

Moein Rahmani[1], Dimitri Galayko[2], Philippe Basset[1], Armine Karami[1,*]

[1]*Univ Gustave Eiffel, CNRS, ESYCOM, F-77454 Marne-la-Vallée, France*

[2]*Sorbonne Université, CNRS, LIP6, F-75005 Paris, France*

*armine.karami@univ-eiffel.fr

***Abstract*—This work presents near-limits kinetic energy harvesting using electrostatic transducers. This concept is based on the active synthesis of the harvester's mass trajectory, to approach the limits of energy conversion from arbitrary types of vibration inputs. It requires that the transducer force is varied in real-time for a specific mass trajectory to be implemented while at the same time collecting the converted energy in the system's energy tank. In this paper, we focus on the problem of selecting the appropriate energy transfer circuit that is responsible for the synthesis of the transducer force. We show and discuss some early simulation results obtained with different such circuits.**

I. Introduction

A major challenge in the design of kinetic energy harvesters (KEH) is to improve the net converted power from non-harmonic and low-frequency mechanical inputs. To this end, we propose an architecture based on the active synthesis of the electromechanical dynamics of the KEH. With this concept that we call "near-limits KEH", the converted energy approaches the physical limit set by the KEH size and the input. Such systems are inherently suited to convert power from low-frequency non-harmonic vibrations, as those found on the human body.

In this paper, we first review the principles of near-limits KEH. We discuss the specific case of systems based on an electrostatic transducer, and we pose the problem of choosing the right electrical interface in this case. We then move on to present early results on testing electrical interfaces of different natures and the challenges posed by their implementation.

II. Principles of Near-Limits KEH

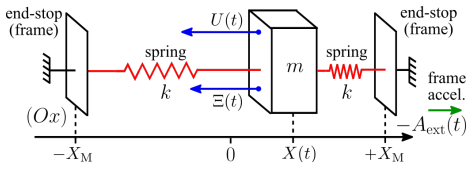

FIGURE 2: SKETCH OF A LINEIC 1-D KINETIC ENERGY HARVESTER.

The model of a lineic, inertial KEH of finite size is depicted in Figure 2. It is governed by the following equation of motion:

$$m\ddot{X} + kX = \Xi(t) + U(t) \qquad (1)$$

with the additional constraint that $|X(t)| \leq X_{\text{M}}$. Here, $\Xi(t)$ and $U(t)$ respectively represent the mechanical input force, and the controller force. The latter converts part of the work done by the former into electrical energy. It can be shown [1] that the maximization of the converted energy is equivalent to the implementation of a specific trajectory for the mobile mass, through this control $U(t)$. This trajectory consists in (i) toggling the mass position from $-X_M$ to $+X_{\text{M}}$, starting and arriving with zero velocity, at minima of the input Ξ (ii) proceeding symmetrically for maxima of Ξ (iii) keeping the mass at the extremal positions $\pm X_{\text{M}}$ in between consecutive extrema of Ξ. Examples of an external forcing and the corresponding optimal trajectory are depicted in Figure 1.

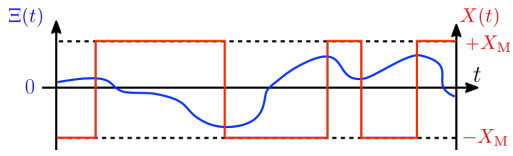

FIGURE 1: EXAMPLE OF AN INPUT $\Xi(t)$ AND THE CORRESPONDING ENERGY-MAXIMIZING TRAJECTORY $X(t)$.

At each local extrema Ξ_0, $U(t)$ should solve the problem

$$\begin{cases} X(0) = \pm X_{\text{M}} \\ X(T_{\text{f}}) = \mp X_{\text{M}} \\ \dot{X}(0) = \dot{X}(T_{\text{f}}) = 0 \end{cases} \qquad (2)$$

subjected to $m\ddot{X} + kX = \Xi_0 + U(t)$ and $|X| \leq X_{\text{M}}$ and where T_{f} is the duration of the toggling. It should be small enough so that $\Xi(T_{\text{f}}) \approx \Xi(0) = \Xi_0$. We suppose in the following that $\Xi(t)$ is positive at its maxima and negative at its minima.

III. Near-Limits KEH with Electrostatic Transducers

Electrostatic transducers offer precise control of the mechanical force through the voltage across them or the charge they carry. Thus, they are a good candidate to implement the transducer force that is needed to implement the optimal trajectory. For an electrostatic transducer, the force reads

$$u(t) = \frac{1}{2}\frac{\partial C}{\partial X}V^2 = \frac{1}{2}\frac{\partial C}{\partial X}\frac{Q^2}{C^2}$$

The capacitor geometry sets the function $C(x)$, while the dynamics of the position X, charge Q, and voltage V are set by the mechanical and electrical dynamics of the system. The mechanical dynamics are governed by the equation of motion (X). The electrical dynamics are set by the electrical circuit connected to the transducer. Therefore, the form of the control force $u(t)$ is constrained by both the transducer capacitor geometry, and the topology of the circuit that sets the dynamics of the electrical variable. Specializing to electrostatic transducers of gap-closing (GC) and area-overlap (AO) geometries, the model (1) becomes, in adimensionalized form

$$\ddot{x} + \Omega^2 x = \Omega^2 \xi_0 + \frac{1}{2}\nu\Omega^2(y_+^2 - y_-^2) \qquad (3)$$

where $y_\pm = q_\pm$ is the non-dimensional charge on the $\pm$ transducer for the GC case, $y_\pm = v_\pm$ is the non-dimensional voltage across the $\pm$ transducer for the AO case. The two transducers are related by $C_+(x) = C_-(-x)$. Both are needed to synthesize forces of two orientations on the (Ox) axis. The parameter $\Omega > 0$ is dimensionless and represents the relative value of the mechanical and electrical resonance frequencies

(see the LC circuit below in Sec. IV). The adimensional variables and parameters are given in Table 1.

TABLE 1: PARAMETERS AND ADIMENSIONAL VARIABLES. $\varepsilon_0\varepsilon_R$ IS THE DIELECTRIC PERMITTIVITY, S, L, W AND D ARE GEOMETRICAL PARAMETERS: TRANSDUCER OVERLAPPING SURFACE, WIDTH, LENGTH AT $x = 0$ AND GAP AT $x = 0$ RESPECTIVELY. OTHER APPEARING PARAMETERS ARE INTRODUCED IN THE TEXT. $\Omega > 0$ IS A FREQUENCY SCALING FACTOR.

ω_0, ξ_0, τ_F	$\sqrt{k/m}$, $\Xi_0/(kX_M)$, $T_F\Omega/\omega_0$
$x(t)$	$X(t\Omega/\omega_0)/X_M$
$C_{0,AO}$, $C_{0,GC}$	$\varepsilon_0\varepsilon_R WX_M/D$, $\varepsilon_0\varepsilon_R S/X_M$
α_{AO}, α_{GC}	L/X_M, $D/X_M > 1$
$C_{AO,\pm}(x)$, $C_{GC,\pm}(x)$	$C_{AO,0}(\alpha_{AO} \pm x)$, $C_{GC,0}/(\alpha_{GC} \mp x)$
$v_{AO,GC}$	$C_{0,AO,GC}V_0^2/(kX_M^2)$
$c_{AO,GC,\pm}(x)$	$C_{AO,GC,\pm}(x)/C_{0,AO,GC}$
$q_\pm$(t)	$Q_\pm(t\Omega/\omega_0)/(V_0C_{0,AO,GC})$
$v_\pm(t)$	$V_\pm(t\Omega/\omega_0)/V_0$

IV. INTERFACE CIRCUITS FOR CONTROL IMPLEMENTATION

In [1], we presented a piecewise-constant control that solves the position toggling problem. The electrical interface considered therein is a bidirectional DC-DC converter, whose switches need to be controlled with precise timing. Here we present other circuits for position toggling with possibly less stringent switch control requirements. We do not consider the problem of removing and setting the keeping force (at $t < 0$ and $t > \tau_F$). Rather, we only focus on the position toggling, and on the recovering of the energy invested into the transducer plus the converted energy. We also do not account for dissipation (electrical or mechanical). The goal is to assess whether a particular circuit architecture can be used to solve (2). By the same account, we do not consider important design constraints, such as the maximum allowable voltage across the circuits' components. We focus on the case $x(0) = -1$, $x(\tau_F) = 1$, i.e., $\xi > 0$. The opposite toggling can be found symmetrically.

A. Toy model: constant voltage and AO transducer

With constant voltage sources of adimensional values $v_{+,0}$ and $v_{-,0}$ connected AO transducers, (2) can be solved. We can suppose here that $\Omega = 1$. In this case the solution to (3) is

$$\begin{cases} x(t) = x_{eq} - (1 + x_{eq})\cos(t) \\ x_{eq} = \xi_0 + \dfrac{v}{2}(v_+^2 - v_-^2) \end{cases}$$

so it suffices to set $v_+ = 0$, and choose v_- in order to have $x_{eq} = 0$. The mass will reach the other end ($x = 1$) with zero velocity at $\tau_F = \pi$, at which time the system must use the other transducer to keep the mass at $x = 1$ (this task is not considered here). The converted energy flows into the constant voltage source. This solution is however unsatisfying, because (i) it can be difficult to implement the voltage source with low consumption (ii) the initial connection and the energy recovery must be done through a dedicated inductive interface that in turn complexifies the control. This is because direct connection of the transducer to the voltage source incurs unscalable losses. Note that using a GC transducer kept at constant charge leads to the same mathematical form as the AO transducer at constant voltage. It is essentially the solution proposed in [1].

B. Inductor and AO transducer

Electrical dynamics arise when the transducer is connected to an inductor. These dynamics read

$$\begin{cases} q_\pm = v_\pm c_\pm(x) \\ \ddot{q_\pm} + \dfrac{q_\pm}{c_\pm(x)} = 0 \end{cases} \quad (4)$$

and $\Omega = \sqrt{LC_{0,AO}}/\omega_0$. The system obtained by combining (3) and (4) is studied by numerical resolution of the coupled ODEs.

We suppose that $q_\pm(0) = q_{0,\pm}$ (a design parameter) at the beginning of each toggling. Figure 3 shows value of x at its first maximum, in terms of the non-dimensional parameters Ω and v. The initial position of the mass is $x = -0.81$, so that systems with first maximum of value $x \approx 0.81$ solve the control problem. As shown in Figure 3, this maximum is independent of Ω unless for $\Omega \approx 1$.

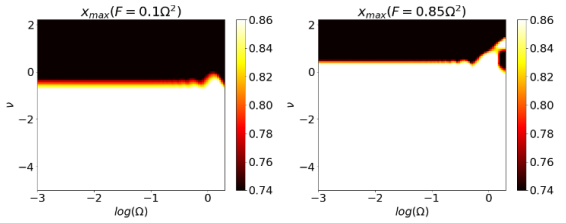

FIGURE 3: FIRST MAXIMUM POSITION THE AO KEH'S MASS VS. Ω AND v FOR TWO VALUES OF THE INPUT FORCE. HERE $F = \xi_0\Omega^2$.

C. Inductor and GC transducer

The same system with a GC transducer is simulated and the results shown in Figure 4. This time the initial position of the mass is $x = -0.9$, so that systems with first local maxima of $x = 0.9$ in the position solve the control problem. We have $\Omega = \sqrt{LC_{0,GC}}/\omega_0$. Here again, the impact of Ω on the peak position is increased for $\Omega \approx 1$.

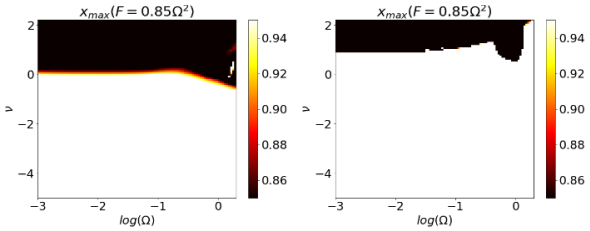

FIGURE 4: FIRST MAXIMUM POSITION THE GC KEH'S MASS VS. Ω AND v FOR TWO VALUES OF THE INPUT FORCE. HERE $F = \xi_0\Omega^2$.

V. CONCLUSION

We presented the near-limits KEH principle with a particular focus on the local mass toggling problem. We focused on the selection of the electrical interface for transferring energy to and from the electrostatic transducer. Our future research will aim at implementing the proposed interfaces in a prototype.

REFERENCES

[1] Karami, A., et al., *Electrostatic Near-Limits Kinetic Energy Harvesting from Arbitrary Input Vibrations.* arXiv preprint arXiv:2002.07086, 2019.